J. Fluid Mech. (2002), *vol.* 454, *pp.* 71–112. © 2002 Cambridge University Press
DOI: 10.1017/S0022112001007182 Printed in the United Kingdom

Vertical structure in stratified wakes with high initial Froude number

By G. R. SPEDDING

Department of Aerospace and Mechanical Engineering, University of Southern California,
Los Angeles, CA 90089, USA

(Received 3 July 2000 and in revised form 24 July 2001)

Initially turbulent bluff body wakes decay in the presence of a stable background density gradient to form chains of comparatively stable and long-lived vortex structures, most of the late-time properties of which have been shown to be independent of the initial generating Froude number (for a sphere of diameter, D, moving at speed, U, $F = 2U/ND$, where N is the buoyancy frequency). Results of experiments with vertical interrogation planes are described, where any anticipated F-dependence might be most evident, as the competing effects of horizontal inertial forcing and the restoring buoyancy force can be measured directly by simultaneous measurement of horizontal and vertical velocity components. Experiments were conducted at sufficiently large values of $Re \geqslant 3 \times 10^3$ and $F \geqslant 4$ that turbulence can occur over many scales in the near wake, and the scaling properties might then extrapolate to ocean engineering applications.

When $F \geqslant 4$, the fluid motions in the intermediate, non-equilibrium régime always occur in coherent patches whose vertical extent is smaller than the total wake height. The patches of vorticity have longer horizontal than vertical coherence lengths, and may be termed layers, even though they are far from uniform in the horizontal. The degree to which the complex vertical structure is later dominated by the mean wake defect depends strongly on F.

The total wake height, L_V, depends on the initial value of F so that $L_V/D \sim F^{0.6}$. L_V is established early and remains almost unchanged up to $Nt \approx 30$. At later times, the non-equilibrium wake exchanges potential with kinetic energy and re-adjusts according to local dynamical constraints, so that, within each layer, the quasi-two-dimensional flow proceeds without any further dependence on, or memory of, the initial value of F. The flow is everywhere stable to overturning Kelvin–Helmholtz instabilities and local length and velocity scales evolve so that the local horizontal and vertical Froude numbers, F_H, F_V, are both of order 0.1.

Although Osmidov-length arguments for vertical scale selection appear to be physically appropriate, they do not correctly predict the measured F-dependence in either L_V, or in the layer height, l_V. Thus the physical mechanism responsible remains elusive, as the alternative laminar instability mechanisms are not presented with the appropriate, scale-free initial conditions over the parameter range in which they have been shown to operate.

Ultimately, the measurements support the application of low F_H and F_V scaling theories to the late wake flow. The preceding non-equilibrium stage, when the vertical structure of the late wake is determined, does not yield so readily to assumptions involving the smallness of the vertical velocity component.

1. Introduction

1.1. *Turbulence in stratified fluids*

The average density gradient in the Earth's oceans and atmosphere is gravitationally stable and episodic turbulence-generating events decay to leave motions that can be significantly affected by the ambient stratification. Due to the inhibition of displacements parallel to gravity, mesoscales in the atmosphere with horizontal scales, $L_H = O(100\text{–}1000\,\mathrm{m})$, and small scales in the ocean ($L_H = O(1\text{–}100\,\mathrm{m})$) typically possess much smaller characteristic length scales, L_V, in the vertical than in the horizontal. The ratio of inertial to buoyancy time scales is measured by an internal Froude number, $F = U/NL$, where the Brunt–Väisälä frequency, $N = \{-(g/\rho_0)(\partial\rho/\partial z)\}^{1/2}$, and L and U are appropriate length and velocity scales. In both naturally occurring geophysical flows and in engineering applications such as the flow behind undersea vehicles, it is common for $F_H = U/NL_H \ll 1$, even when the initial value of F, set by the turbulent generating conditions, is high (the H subscript will be used to denote quantities defined in the horizontal plane, and the V subscript is used for quantities in the vertical direction, parallel to the direction of the gravitational force). The way in which a flow adjusts to the constraining influence of the stratification when $F_V \leqslant 1$ is critical in determining the late-time dynamics, when F_V is frequently considered to be small. A fine review of the strongly stratified limit can be found in Riley & Lelong (2000).

1.2. *Low Froude number theory*

A low Froude number theory was first constructed by Riley, Metcalfe & Weissman (1981) and Lilly (1983). The Navier–Stokes equations for a Boussinesq fluid are non-dimensionalized by scaling horizontal and vertical directions as $x \sim L_H$, $z \sim L_V$ and horizontal velocities by the horizontal, fluctuating velocity, $u \sim u'$. Time is scaled by the advective time scale, $t \sim L_H/u'$, and the pressure and density are scaled by $p \sim \rho_0 u'^2$ and $\rho \sim \rho_0 u'^2/L_V g$, where ρ_0 is the mean density. In the limit $F_V = u'/NL_V \to 0$, and ignoring viscous and diffusive effects, the lowest-order equations for the velocity field become

$$\frac{\partial}{\partial t}\boldsymbol{u}_H + \boldsymbol{u}_H \cdot \nabla \boldsymbol{u}_H = -\nabla_H p, \tag{1.1}$$

and

$$\nabla_H \cdot \boldsymbol{u}_H = 0. \tag{1.2}$$

Vertical and horizontal motions are decoupled at this order, but vertical variation of the two-dimensional velocity fields can occur. The lowest-order horizontal motions have no Froude number dependence. The vertical velocity, w, is scaled as

$$w \sim u'\alpha F_V^2,$$

where $\alpha = L_V/L_H$ is the aspect ratio; w appears at order F_V^2 and couples the pressure and density,

$$0 = \frac{\partial p}{\partial z} - \rho, \tag{1.3}$$

$$\frac{\partial \rho}{\partial t} + \boldsymbol{u}_H \cdot \nabla\rho - w = 0. \tag{1.4}$$

The vertical pressure gradients originating in (1.1) are balanced by variations in the density field (1.3), which in turn are achieved through small vertical velocities in (1.4). The precise low-F scaling arguments can be found as originally derived in Riley *et al.* (1981). They are reviewed in Riley & Lelong (2000), and derived more formally in Embid & Majda (1998). The equations have been very successful in understanding observed low-F dynamics in laboratory experiments, and in particular, the lowest-order equation for the vertical vorticity,

$$\frac{\partial}{\partial t}\omega_z + \boldsymbol{u}_H \cdot \nabla \omega_z = 0, \tag{1.5}$$

again omitting the diffusion term, demonstrates that the vorticity following a fluid element is conserved. The enhancement of horizontal scales and slow time variance of coherent patches of vertical vorticity, together with the possible co-existence of vertical shearing between quasi-two-dimensional layers are all dynamical features of these reduced equations. Majda & Grote (1997) showed that the simultaneous appearance of horizontal vorticity and vertical shearing is an intrinsic property of the low-F equations, and this too appears to reflect the behaviour of real stratified flows, where vertical shearing between slowly varying vortical modes is an important source of kinetic energy dissipation, as detailed in the laboratory and numerical experiments discussed below. The non-propagating component of motion is more properly associated with the potential vorticity, which is a conserved quantity along fluid element trajectories. Analysis of the PV mode (following the nomenclature of Riley & Lelong 2000) was generalized to the non-flat, isopycnal reference frame by Staquet & Riley (1989) and an extension to weakly nonlinear wave–vortex interactions was given by Lelong & Riley (1991).

Equations (1.1)–(1.4) have solutions that contain dynamics similar to that observed in experiments at late times when the local Froude number is presumably, or measurably, small. The scaling in fact requires that both F_H and F_V be small, and this can be tested in experiments that measure both velocity components simultaneously. The low-F equations contain the possibility of vertical variability in the primarily horizontal motions, but a preferred vertical length scale, if one exists, is not determined, and the precise nature of the coupling between adjacent horizontal layers is also not resolved.

1.3. *Numerical simulation*

Developing anisotropy can also be verified in numerical experiment, and indeed the original scaling by Riley *et al.* (1981) was suggested by findings in a direct numerical simulation of a Boussinesq fluid in a 32^3 box. The simulations showed, amongst other things, a decrease in total energy decay rate with increasing stratification, the increasing magnitude (with time) of the horizontal vorticity component with respect to the vertical component, and the increasingly small value of locally defined turbulent Froude numbers, particularly in the more strongly stratified case.

The frictional effects of layering in strongly stratified flows were noted by Herring & Métais (1989) and Métais & Herring (1989) for forced and freely decaying simulations, respectively. In the freely decaying case, the final flow state depended on the initial conditions which varied in their partition between vortical and wave modes. F_V began with values around 1, and decreased after 20–30 initial eddy turnover times to 0.3–0.6, and while horizontal integral scales grew with time, the vertical scales grew only very slowly.

Kimura & Herring (1996) computed a DNS of decaying stratified turbulence, this time with a resolution of 128^3. The suppression of vertical displacements by stratification and the evolution of pancake vortices of moderate aspect ratio, together with the increasingly horizontal mean vorticity vector orientation, were all consistent with the emerging picture of strongly layered late-time dynamics.

While some degree of vertical structure can be observed in all of these simulations (particularly in Herring & Métais 1989, figures 10 and 11), no explicit preference for any particular vertical scale is discussed.

1.4. *Laboratory experiments: grid turbulence*

Laboratory experiments do not have modelling difficulties at small scales, but practical considerations usually limit the available Reynolds numbers, *Re*, and F range. Nevertheless, it is laboratory experiments that have lead the way in identifying the major emerging coherent structures, one of the most evident properties of which is their high aspect ratio ($A = L_H/L_V = 1/\alpha$), earning the label 'pancake vortices'. Some detailed consideration has been given to what determines their vertical extent.

Several studies have investigated the evolution of grid turbulence from this point of view. Hopfinger (1987), Browand, Guyomar & Yoon (1987) and Liu, Maxworthy & Spedding (1987) all observed the emergence of a preferred vertical scale at some equivalent distance from a high-F, high-*Re* (based on grid mesh scales) source. It is reasonable to argue that vertical length scales are limited by a local dynamical constraint on the kinetic energy available to move a fluid element a given distance away from its equilibrium position in the mean density gradient. In fully developed turbulence, the overturning (Osmidov) scale, l_o, can be written

$$l_o = \left(\frac{\epsilon}{N^3}\right)^{1/2} = \left(\frac{u'^3}{lN^3}\right)^{1/2}, \tag{1.6}$$

where l is a turbulent integral length scale. At sufficiently high F, the turbulence does not immediately feel the effects of the background stratification, and integral length scales grow equally in all directions. When l reaches l_o, as the available kinetic energy decays, either with time or with increasing distance from the source, further increase in vertical scale is impossible; l_o continues to fall, and the initial point when $l \approx l_V \approx l_o$ marks the maximum vertical scale of disturbances that can be preserved in the flow. If the average density gradient has been mixed within l_V, then motions with vertical scales up to l_V may continue for long enough to establish $l_V = L_V$ as the largest characteristic vertical scale of coherent motion in the flow. Horizontal length scales, on the other hand, are free to increase, and the anisotropy in length (and velocity) scales begins.

In their oscillating grid experiments, Browand *et al.* (1987) showed how inserting empirically determined scaling laws for the downstream evolution of length and velocity scales for non-stratified grid turbulence would lead to a $L_V \sim (\omega/N)^{1/2}$ behaviour (where ω is the grid oscillation frequency), and confirmed this dependence in their experiments. The success of this result, achieved over more than an order of magnitude variation of ω/N was considered strong support for the original postulate of Osmidov.

However, as noted by Hopfinger (1987), Browand *et al.* (1987) and Liu *et al.* (1987), measured intrusion heights in layers formed by collapsing grid turbulence significantly exceed the Osmidov scale, typically $L_V \simeq 7l_o$. Liu *et al.* (1987) offered an explanation based on competitive inhibition between immediate neighbouring layers, analogous to that observed in Hele-Shaw cells, and this assertion has yet to be tested. As also noted by these authors, the correct explanation must take into account the large-scale horizontal motions evolving in each layer, and the physical argument must be regarded as incomplete.

The coherent patches of vertical vorticity that characterize the almost horizontal motions in a stably stratified fluid have been investigated by Voropayev, Aranasyev & Filippov (1991) and Voropayev & Afanasyev (1994), mostly by tracing the evolution of patches of dyed fluid introduced at or near the source at low or moderate *Re* and *F*. Fincham, Maxworthy & Spedding (1996) made accurate, quantitative estimates of the fluid motions in separate isopycnal (nearly horizontal) and vertical planes in the decaying turbulence generated by a towed array of vertical flat plates, and found the correspondence between the strong shearing across horizontal vortex sheets between separate layers, each of which is characterized in the horizontal by the emergence and persistence of large-scale coherent patches of vertical vorticity. These vortices are in no sense isolated from each other, contrary to those observed in purely two-dimensional turbulence simulations (cf. McWilliams 1984), because vortex lines can connect in closed loops as ω_z components can bend over to form the increasingly strong ω_H interlayer sheets. Shearing between the layers was estimated to account for nearly 90% of the total kinetic energy dissipation.

The predicted topology of the vortex lines was confirmed in the numerical simulations of Kimura & Herring (1996), and the necessary linkage between the increase in the relative contribution of ω_H and dominance of $\partial \boldsymbol{u}_H/\partial z$ terms in the viscous dissipation can be explained by the analysis of Majda & Grote (1997). It should further be noted that all of these features are quite consistent with the earlier numerical simulations of Riley *et al.* (1981) and Métais & Herring (1989), and with the scaled equations (1.1)–(1.4).

1.5. *Laboratory experiments: bluff body wakes*

The comprehensive review of Lin & Pao (1979) and data cited therein on the emergence of large-scale structures in the wake of towed and self-propelled submerged bodies stimulated much of the research in stratified turbulent flows. That body of work has now been significantly augmented by the very careful shadowgraph-based methods of Sysoeva & Chashechkin (1991), the comprehensive range of *Re* and *F* covered in dye and streak photography of Lin *et al.* (1992), the combined hot-film and novel fluorescein dye-sheet techniques of Hopfinger *et al.* (1991), Chomaz, Bonneton & Hopfinger (1993*b*), Bonneton, Chomaz & Hopfinger (1993) and Bonneton *et al.* (1996), and by quantitative particle tracking or DPIV-based methods (Chomaz *et al.* 1993*a*, Spedding, Browand & Fincham 1996*a*, *b* and Spedding 1997). The experimental results are reviewed in Spedding (1999). Most of the quantitative information on the vortex wake and its induced velocity field concentrates on the horizontal motions in the far wake. Chomaz *et al.* (1993*a*) measured a progressive decoupling of neighbouring horizontal layers in the towed sphere wake when the body Froude number exceeded 4–4.5, and Spedding *et al.* (1996*b*) conjectured that the vertical structure of multilayered wakes ought to have preferred vertical offset locations at late times. Preliminary data in Spedding (1999) showed $\omega_y(x, z)$ distributions in single, vertical, centreline slices, indicating that the somewhat disorderly stacking of layers in the real wake might resist such simplification for $F \geqslant 4$.

All initially turbulent (three-dimensional) wakes were found to have an intermediate non-equilibrium régime (NEQ) that is characterized by decreased kinetic energy dissipation rates, and that precedes a later quasi-two-dimensional (Q2D) régime where vertical motions are certainly small, and may or may not be validly treated as vanishingly small. The decreased kinetic energy decay was proposed to be related to the reconversion of potential to kinetic energy as displaced fluid parcels readjust to their stable equilibrium position in the density gradient. The timing and direction of this energy transfer is just as predicted in the early numerical simulations of Riley *et al.* (1981) and Métais & Herring (1989). Vertical velocities associated with this process should be measurable, but to date have not. It was proposed that the physical mechanisms operating in the NEQ regime ought to be quite general, applying to any freely decaying turbulent patch in a stable density gradient. The transition from 3D → NEQ → Q2D in decaying, stably stratified flows bears a passing similarity with the passage from active – active-fossil – fossil turbulence in the hydrodynamic phase diagrams of Gibson (1986, 1991), but, as Riley & Lelong (2000) point out, the PV mode in the low-F equations (1.1)–(1.5) does not fit easily into a category that is described as 'inactive' and 'completely fossilised'.

1.6. *Objectives*

Decaying turbulence in a stably stratified fluid displays a broad range of dynamics as the flow regime transitions from fully three-dimensional turbulence to buoyancy dominated quasi-two-dimensional motions. The degree to which the late-time dynamics can adequately be described by layers of two-dimensional Euler equations depends on the differing vertical and horizontal length scales that emerge during this period, and the rôle of a small, but non-zero, vertical velocity component can also be investigated. Despite the fact that the initially turbulent wake has many engineering and geophysical applications (as an example of the evolution of a turbulent patch in an otherwise quiescent, but stratified environment), no quantitative information is available on the simultaneous time evolution of the vertical and horizontal velocity components in the evolving wake.

The objectives of this paper are to provide a quantitative description of the vertical wake structure that complements the previous isopycnal/horizontal plane information presented in Spedding *et al.* (1996*b*) and Spedding (1997) (henceforth denoted SBF96 and Sp97) and to capitalize on the simultaneous measurement of velocity components both normal (parallel to the flow forcing) and parallel to gravity. The calculated structure aspect ratio and associated horizontal and vertical Froude numbers that establish initial conditions for the late-wake Q2D flow, bear directly on the applicability of the low-F scaling described in § 1.2. Accurate estimation of the spatial velocity gradients can be combined with previous horizontal plane data to draw up an energy budget for the decaying wake. Most of the data will be concentrated in the NEQ and early Q2D régimes ($5 \leqslant Nt \leqslant 100$), where the readjustment from disordered, fully three-dimensional motion occurs under the constraining influence of the buoyancy force to produce the long-lived and stable pancake vortex configurations. The focus will be on the emergence of these ordered flows from initially turbulent conditions, requiring moderate to high (within laboratory constraints) values of $Re \geqslant 5 \times 10^3$ and $F \geqslant 4$.

2. Experiments

2.1. *Particles and lighting*

Experiments were conducted in a 2.4 × 2.4 m square tank with 1.4 m startup section, details of which may be found in SBF96. Illumination in a vertical plane is provided by a 5 W argon laser. The beam is spread in one direction by reflection off the front face of an oscillating mirror. Without any special intervening optics, the laser sheet thickness is approximately 4 mm. The sheet penetrates the continuously stratified (close to linear, as produced by the standard two-tank filling method) water perpendicular to its surface. If the surface is free of particulate contaminants, the illumination is quite uniform across its width, apart from the edges (the mirror is driven by a 200 Hz sine function) which are kept outside the imaged area. Particles are 50 μm diameter plastic-encapsulated rhodamine, introduced at the surface over the whole tank and allowed to settle for about 2 hours before experiments are conducted. The natural range of particle settling speeds gives a reasonable particle density over the image area for about the next 2 hours.

2.2. *Flow imaging*

Particle images in the vertical plane were captured on a CCD camera contained in a waterproof submerged box placed 1 m from the centreline. This distance marks a compromise between reducing physical interference of the box with the wake-induced flow (including effects of local separations at the sharp corners of the box) and avoiding excessive non-uniform optical refractions at local density gradients which are integrated along the light path from particle surface to CCD array. In a tank of this size, it is difficult to mix fluids with refractive index matching, and so a degree of image distortion is unavoidable. The magnitude of the measurement error depends not only on the apparatus geometry and density gradient at rest, but also on the local, time-varying flow properties, so a meaningful calibration is impossible without either prior knowledge of the flow field to be measured, or interleaved control information separated from the flow data by time scales that are short compared to wake turbulence or eddy turnover time scales. Here, the measurement uncertainty due to viewing through non-uniform density gradients was estimated in control experiments by measuring the apparent motion of stationary particles glued to a flat black background which was placed 10 cm behind the vertical centreline. The signal to noise ratio in both maximum fluctuating velocity magnitude and gradient quantities was between 8 and 10 for $10 \leqslant Nt \leqslant 200$. This is, at first sight, a small number, but it is derived through refraction through both sides of the wake (and so a more realistic ratio will be at least twice this number). Moreover, the integrated effect across the wake (or half of it) has very little phase correlation, and the random, small-scale fluctuations introduced are easy to filter from the main signal. The filtering is achieved primarily by a fourth-order Butterworth low-pass filter applied to the velocity field following interpolation. Nevertheless, the large initial disturbances to the background density gradient, together with the magnitude of the out-of-plane velocity component, comprise the principal constraints on the earliest possible data acquisition times.

3. Analysis and interpretation

3.1. *Parameter range*

This paper describes experiments where a sphere of diameter D is towed horizontally at speed U through a fluid of uniform density gradient, with constant buoyancy frequency, N. The governing parameters are the internal Froude number, $F = 2U/ND$, and the Reynolds number, $Re = UD/\nu$, where ν is the kinematic viscosity calculated at the mid-height, $z = H/2$ where $\rho = \rho_0$.

Some 46 separate experiments were conducted with $0.50 \leqslant N \leqslant 1.58$ (rad s^{-1}), $0.64 \leqslant D \leqslant 5.08$ (cm) and $16.0 \leqslant U \leqslant 81.3$ (cm s^{-1}). Appropriate combinations allowed the design of independent variations in $F \approx [4, 16, 64, 128, 256, 512]$, $Re \approx [5, 10, 20 \times 10^3]$ and $D/H \in [0.03, 0.21]$, as shown in table 1.

Confinement effects as measured by variations in D/H are not explicitly treated here, except insofar as the results can be verified to be unaffected. Five further experiments were run in homogeneous, fresh water. The technique required no modification,

F	4	16	64	$Re = 8 \times 10^3$
$y/D = 0$	●	●	●	
1	●	●	●	
3.5	●	●	●	

F	57	128	256	512
$Re(\times 10^3) = 5$	●	●	●	●
10		●		
20		●		

TABLE 1. F and Re ranges covered in vertical slice experiments designed to investigate independent variation in either parameter, when both are high. The symbol indicates that one or more experiments were conducted. In the lower half, all data were taken at the vertical centreplane, $y/D = 0$.

but the maximum measurement time was greatly reduced owing to the lack of the usual buoyancy-induced constraints on the vertical wake growth. Three experiments were conducted with a ‘null sphere’ (simply a wire knot in place of the sphere) to measure the effects of the support wire wakes.

3.2. *CIV measurements of* $\{u, w\}(x, z, t)$

Velocities in the vertical measurement plane were calculated with the correlation imaging velocimetry (CIV) technique described by Fincham & Spedding (1997). Previous use of this method in the stratified wake experiments exploited the fact that fluid motions ($\boldsymbol{u}_H = \{u, v\}$, projected onto $\{x, y\}$) at moderate Nt on almost-horizontal isopycnals could be separated into vortical and wave components

$$\omega_z = \nabla \times \boldsymbol{u}_H, \quad \Delta_z = \nabla \cdot \boldsymbol{u}_H. \tag{3.1}$$

Now, the measurable velocity components are $\boldsymbol{q} = \{u, w\}$, with magnitude $q = |\boldsymbol{q}|$, and the local shearing motions in the $\{x, z\}$ plane are measured by the horizontal vorticity

$$\omega_y = \nabla \times \boldsymbol{q} \tag{3.2}$$

which combines contributions from what previously could be separately diagnosed as wave and vortex modes (3.1), and later on from vertical shearing between adjacent layers. Although periodic propagating modes can readily be labelled as internal waves, close to the wake centreline the distinction in experiment between wave and vortex modes at early times is neither obvious nor useful.

3.3. *Mean and fluctuating velocity components*

u and w are normal and parallel, respectively, to the direction of the restoring buoyancy force, and in comparing their magnitudes, it can be useful to distinguish between horizontal motions that are part of the mean wake defect profile, and those that are fluctuations about this mean. The streamwise-averaged profiles $U_X(z)$ are calculated, where U_X at each z is the mean value of u over the observation window length in x, ΔX. The fluctuating component of u, excluding the mean profile is

$$u'(x, z) = u(x, z) - U_X(z). \tag{3.3}$$

Removing $U_X(z)$ is equivalent to removing a steady mean flow component from a fixed probe that averages over a time $T = \Delta X / U_X(z)$. Similarly, a fluctuating horizontal vorticity can be defined as

$$\omega_y' = \frac{\partial w}{\partial x} - \frac{\partial u'}{\partial z}; \tag{3.4}$$

ω_y' is the part of the shearing motion that is not directly due to the mean wake profile. The prime notation will be used for all quantities based on $u'(x, z)$.

3.4. *Estimating the kinetic energy dissipation rate*

The rate of dissipation of kinetic energy per unit mass is

$$\epsilon = -2\nu \overline{s_{ij}s_{ij}}, \tag{3.5}$$

where the elements of the strain rate tensor, s_{ij},

$$s_{ij} = \frac{1}{2}\left(\frac{\partial u_i}{\partial x_j} + \frac{\partial u_j}{\partial x_i}\right), \tag{3.6}$$

are summed over the indices $i, j = 1, 2, 3$, each representing a component parallel to the Cartesian coordinate axes, $\{x, y, z\}$. The overbar in (3.5) usually denotes a time average. Here it is used to denote a spatial average at one instant in time. Statistical averages in an inhomogeneous flow are functions of location, and so the domain must be specified appropriately if they are to have any meaning (see below).

Consider now the dissipation in the $\{i, j\}$ plane, normal to k. The contribution of in-plane velocity gradients to the total dissipation can be written by multiplying out the terms of (3.5) and so, omitting the minus sign,

$$\begin{aligned}\epsilon_k = \nu \Bigg\{ & 2\overline{\left(\frac{\partial u_i}{\partial x_i}\right)^2} + 2\overline{\left(\frac{\partial u_j}{\partial x_j}\right)^2} + \overline{\left(\frac{\partial u_i}{\partial x_j}\right)^2} + \overline{\left(\frac{\partial u_j}{\partial x_i}\right)^2} \\ & +2\overline{\left(\frac{\partial u_i}{\partial x_j}\frac{\partial u_j}{\partial x_i}\right)} + 2\overline{\left(\frac{\partial u_i}{\partial x_j} + \frac{\partial u_j}{\partial x_i}\right)\left(\frac{\partial u_i}{\partial x_i} + \frac{\partial u_j}{\partial x_j}\right)}\Bigg\}. \end{aligned} \tag{3.7}$$

In isotropic turbulence, or in any plane with mean zero divergence in the plane, the last term of (3.7) drops out to yield

$$\epsilon_k = \nu \left\{ 2\overline{\left(\frac{\partial u_i}{\partial x_i}\right)^2} + 2\overline{\left(\frac{\partial u_j}{\partial x_j}\right)^2} + \overline{\left(\frac{\partial u_i}{\partial x_j}\right)^2} + \overline{\left(\frac{\partial u_j}{\partial x_i}\right)^2} + 2\overline{\left(\frac{\partial u_i}{\partial x_j}\frac{\partial u_j}{\partial x_i}\right)}\right\}. \tag{3.8}$$

The last term of (3.7) also vanishes when the plane strain and divergence terms are uncorrelated over the averaging operation. In practice, we make the simplifying assumption that spatial averaging over wake and outer flow domains (defined in the following section) allows the simple form of (3.8) to be retained, and in the current experiments the small magnitude of the difference between (3.7) and (3.8) can be experimentally verified. The total dissipation is thus approximated by piecing together information from separate horizontal and vertical cuts through the flow field, as shown in figure 1(*a*). When averaged over the wake domain alone, the shortened notation $S_k = \langle \epsilon_k \rangle_W$ is used.

The velocity gradients measured from separate experiments in the horizontal and vertical planes are shown in figure 1(*b*). Of the six independent terms in s_{ij}, only $s_{23} = \frac{1}{2}(\partial v/\partial y + \partial w/\partial y)$ is missing, but cross-products in (3.5) from different (horizontal and vertical) experiments cannot be calculated directly.

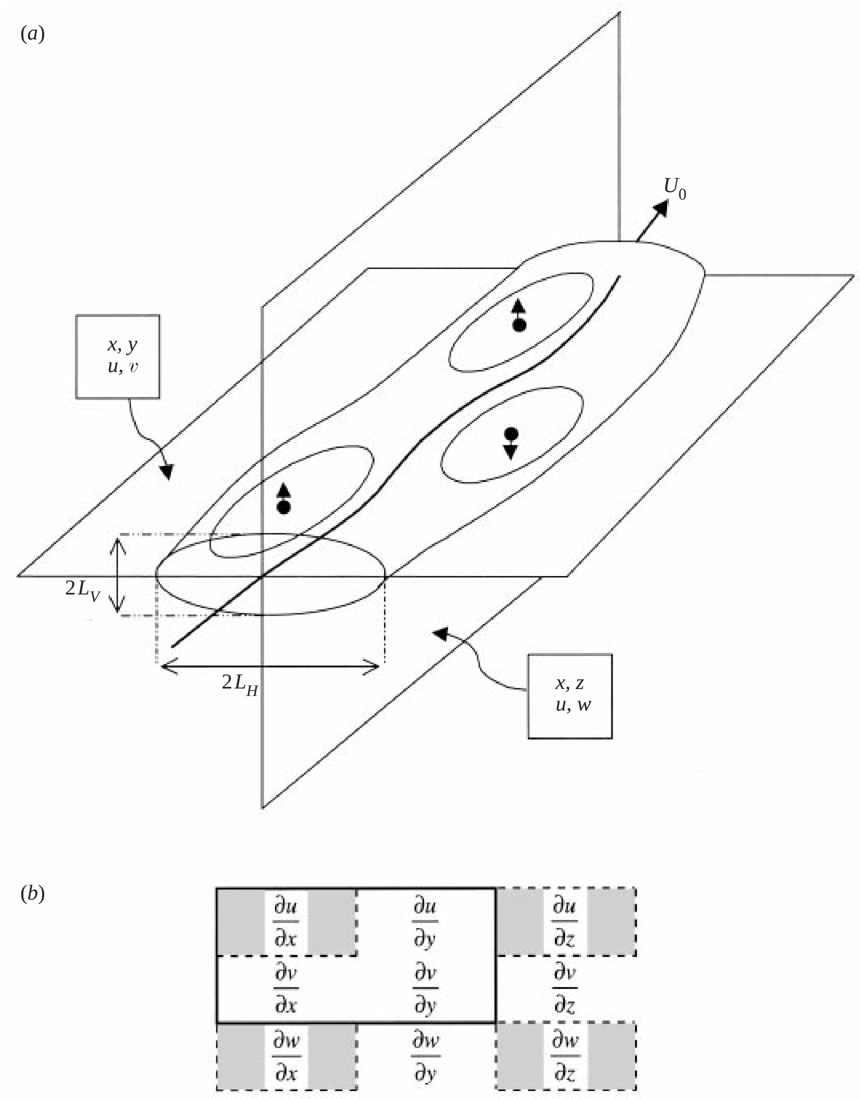

$\frac{\partial u}{\partial x}$	$\frac{\partial u}{\partial y}$	$\frac{\partial u}{\partial z}$
$\frac{\partial v}{\partial x}$	$\frac{\partial v}{\partial y}$	$\frac{\partial v}{\partial z}$
$\frac{\partial w}{\partial x}$	$\frac{\partial w}{\partial y}$	$\frac{\partial w}{\partial z}$

FIGURE 1. (*a*) Simplified model of a stratified wake and its measurement. Wake-averaged quantities are taken over a finite streamwise length, within an elliptic cross-section tube of characteristic horizontal and vertical scales, $2L_H$, $2L_V$. Ensemble averages can be collected from separate experiments in horizontal and vertical planar measurements, as shown. Making such measurements requires no particular assumptions concerning further details, such as the topology of vortex interconnections or presence or number of vertical layers. (*b*) Shear and normal strain rates available from horizontal (upper left square) and vertical measurement planes (dashed lines). $\partial u/\partial x = s_{11}$ is available from both.

3.5. *Definition of wake and outer flow*

As shown in figure 1(*a*), and analagous to the convention established in the horizontal plane studies, a wake region is defined as the vertical band in z where $U_X(z) > 0.2U_0$, and U_0 is the maximum of $U_X(z)$. The flow is separated into two regions, a wake flow and a far field, bounded by an ellipse whose horizontal and vertical axis lengths are determined by the mean wake widths averaged over ΔX. Spatially averaged quantities that are confined to to the wake region are denoted by $\langle\rangle_W$, while unsubscripted angular brackets apply to the entire observation box.

3.6. *Two-dimensional slices through three-dimensional flows*

In contrast with the previously reported isopycnal method for measuring $\boldsymbol{u}_H$ in almost-horizontal isopycnal planes at moderate to late Nt, in vertical slices through the same flow field, there is no tendency for the flow to limit the magnitude of the out-of-plane velocity components compared with the in-plane component. Consequently it is just as likely that three-dimensional structures (streamlines, vortex lines, coherent 'structures') will (*a*) have significant variation in the out-of-plane direction (here the y-axis), and (*b*) will be moving with respect to this reference frame. Disregarding for now the more complex question of how to even define a vortex, or coherent structure (e.g. see Dallmann, Vollmers & Su 1999 for further discussion) it is easy to see that the choice of both reference frame and slice orientation affect conclusions concerning the possible existence of flow structures sampled in only one plane. Three reasonable precautions may be taken: (i) In qualitative descriptions of wake structure, make as few assumptions as possible concerning the unknown extension of flow structures outside the observation plane. (ii) Consider quantitative measures of velocity components, and their gradients, as projected onto the (x, z)-plane. This plane is not completely arbitrary, since x and z are parallel to the sphere trajectory and the gravitational vector, respectively. (iii) When necessary, compare projected patterns of flow quantities with predictions from simple models. In particular, based on the conjectured three-dimensional structure of SBF96, one might compare two cases: one in which vortices in multiple layers remain correlated in the vertical, and one in which they are exactly π out of phase. Figure 2 shows cartoons of such wakes, and the likely flow pattern in vertical cuts through them.

4. Results

4.1. *The basic flow field*

4.1.1. *The horizontal vorticity field, $\omega_y(x, z)$ for $F = 4, 16, 64$*

The normal components of the three-dimensional vorticity fields in vertical slices at, and off the centreline is shown in figures 3 (with its associated velocity field in figure 4), 5 and 6. Full numerical details are given in the captions, and in figures 7 and 8, which effectively plot the colour bar scaling, $|\omega_y|_{max}$, at each timestep, for each case. Reference will be made to frame numbers, or timesteps, numbered 1–12, regardless of whether a particular spot is empty. The emphasis in CIV analysis is on the correct estimate of steep gradient quantities, and this is achieved at the expense of some systematic errors in far-field, low-gradient regions, such as in figure 3(*b*), frames 1–3 and 8.

When $F = 4$, the flow is fully turbulent at first ($Re \simeq 8 \times 10^3$), and commonly presumed to be unaffected by stratification, up until $Nt \simeq 2$. The three time series in figure 3 begin only at $Nt = 8$, and so it is unsurprising to see anisotropy at this time. (Further details of the development of anisotropy in mean and turbulence profiles are given in Spedding 2001) The time series covers roughly the NEQ wake-readjustment period in the top two rows, with a nominally quasi-two-dimensional phase in the bottom row. The vertical structure is quite non-uniform with signs of thin patches of concentrated horizontal vorticity, tilted nose-down in the direction of the mean flow (left to right). Qualitatively, there is no sign of a wake collapse (none would

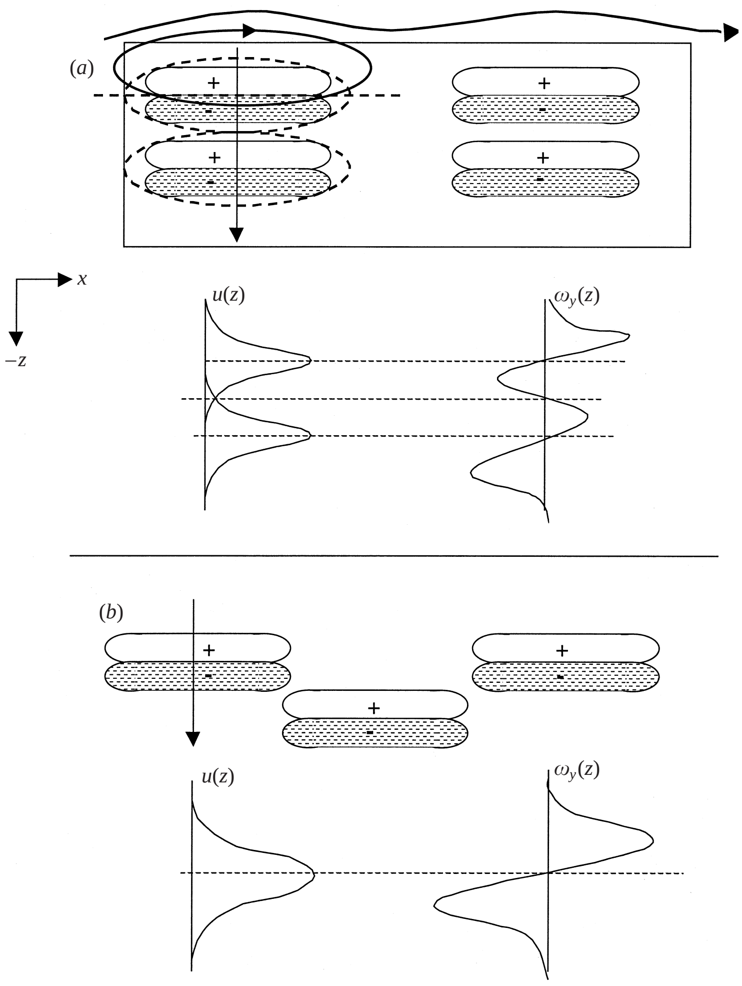

FIGURE 2. Cartoons of predicted out-of-plane vorticity, $\omega_y(x, z)$, distribution on a vertical sheet that cuts through the outer edge of a section of wake composed of vortex structures that are: (a) vertically stacked, and (b) vertically offset. The three-dimensional topology is denoted by bold lines in (a), and the predicted $u(z)$ and $\omega_y(z)$ single drop profiles are shown for each case. Although both are nominally two-layer topologies, the number of peaks and zero-crossings in $u(z)$ and $\omega_y(z)$ are different.

be expected at this late Nt) in the sense of a reduction in vertical wake extent, but the vertical growth rate is evidently very slow, after early wave-like disturbances have propagated away from the centreline. Ultimately, the centreline flow comes to be dominated by the mean wake defect, marked by two almost-horizontal layers of opposite-signed vorticity.

The data off the centreline are more interesting. At $y/D = 1$ (figure 3b), the first vortical (in the sense of high ω_y) structure to impinge upon the measurement plane looks like the flow induced by one or two coherent structures. In the laboratory-fixed reference plane, the mean flow direction is from left to right, so light patches lie above dark patches, just as in the mean wake (figure 3a). The entire top row (up to $Nt = 32$) has significant internal wave signatures that do not appear simply as a background field upon which the remainder is superimposed, but rather as coupled with the thin

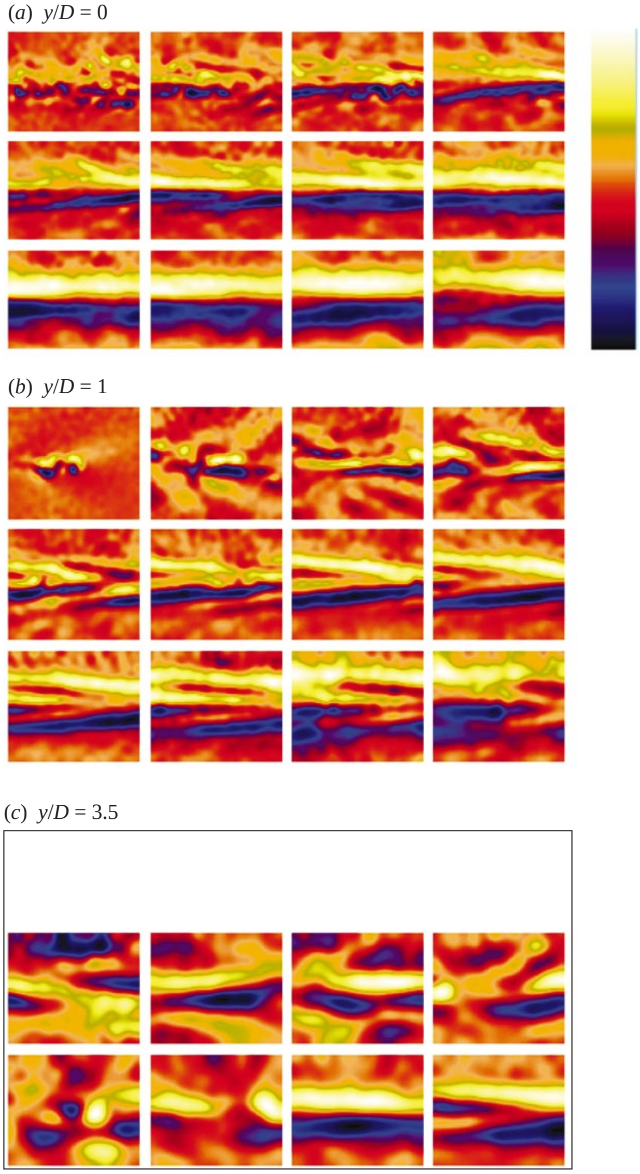

FIGURE 3. $\omega_y(x, z, Nt)$ for $F = 4$ and $y/D = \{0, 1, 3.5\}$ in (*a*), (*b*) and (*c*). At $t = 0$, the sphere was at $\Delta X/2$, moving from left to right. The timesteps are coincident in each ($y/D =$ const.) series, $\pm 3Nt$, and are at $Nt = \{8, 15, 23, 32, 42, 54, 67, 81, 97, 114, 133, 155\}$. The conversion to x/D can be made from the correspondence, $x/D = NtF/2$, which here is $2Nt$. For $y/D = 3.5$, no coherent signal can be distinguished above the noise before $Nt = 42$. At each timestep, the colour bar (upper right) is rescaled locally, and symmetrically, about $\omega_y = 0$ to $\pm|\omega_y|_{max}$. $|\omega_y|_{max}$ *vs.* Nt is plotted in figure 7. The field of view is not the same in different slices. For $y/D = \{0, 1, 3.5\}$, $[\Delta X/D, \Delta Z/D] = [2.20, 1.36], [2.02, 1.65], [1.67, 1.35]$.

and intense shear layers marking the edge of the growing wake. Each shear layer pair can be inferred to be a cross-section through the previously measured pancake eddies which are cohering during this development phase (SBF96, Sp97).

There are clear indications in the $y/D = 1$ data of figure 3(*b*) that more than one pair of shear layers appears in the vertical. It is more evident than at $y/D = 0$ because the measurement is less dominated by the mean wake defect. The vertical layering persists into the Q2D régime (bottom row), but now the layers themselves thicken and merge, presumably by viscous diffusion. A layer can be defined as a pair of shear layers of opposite-signed vorticity, with zero or more neighbours in the vertical direction, and whose nearest shear layer is also of opposite sign. Usually, some minimum or regular horizontal extent is implied, but no such restriction or assumption is incorporated into the working definition above, and the neat, orderly stacking of models such as figure 2 can already be seen to be mostly mythical.

The off-centreline vorticity fields show a wide variety of patterns in $\omega_y(x, z)$ as three-dimensional structures intersect the vertical plane, and the wake grows horizontally through it (figure 3*c*). When a measurable signal is present at $y/D = 3.5$, it is present everywhere, and the distinction between wave and vortex modes cannot easily be made, even at quite late times (lower left panel, $Nt = 92$). The interpretation is not so easy, but a vector plot (figure 4) of the same data as figure 3(*c*) can assist.

The first five panels (*a–e*) in figure 4 are equivalent to frame numbers 3, 5, 7, 9 and 11 in figure 3(*c*). The first disturbance to reach the measurement plane covers the whole observation window, has almost no ω_y (normal to the plane of measurement; thus it is absent in the top row of figure 3*c*), and is almost all vertical motion, symmetric about z_0. It is most likely a lee wave, formed at the sphere itself, and which appears right at the edge of the turbulent wake at this value of F. The familiar arguments concerning the diminishing importance of the lee wave field as $F \geqslant 4$ (e.g. Bonneton *et al.* 1993; Spedding *et al.* 1996*a*) are not incorrect, but it is also notable that as F increases, so the lee waves make an increasingly shallow angle with the wake centreline, and $F = 4$ marks the boundary where the lee waves and internal waves generated at the horizontal wake boundary are almost indistinguishable. When $F > 4$, the lee wave field is immersed in the turbulent wake itself.

A return flow (from right to left) can be seen in figure 4(*b*), where regions of almost horizontal motion are emerging. They appear at different z levels simultaneously. The mean flow direction is opposite to the mean wake, as though cut through the outer edge of one or more recirculating horizontal eddies. As the wake continues to expand horizontally, it self-samples, passing through the stationary light sheet, and complex recirculating regions can be seen (panels *c* and *d*), coupled with motions that have coherent structure out into the far field, and are almost certainly wake-generated waves. Finally, in the bottom row, the mean wake cuts the light slice, and a more simple structure appears, although still not completely uniform, as indicated by the return flow in figure 4(*f*).

The off-centreline vertical slices indicate a coupling between wave and vortex motions. Moreover, it is clear that w cannot be considered small until at least $Nt \geqslant 100$. Up until this time, attempts to enforce this condition, either experimental or numerical, will fail to represent the flow.

The further variation in $\omega_y(x, z)$ with increasing F is shown in figures 5 and 6. For $F = 16$ (figure 5), a larger-scale undulation initially appears on the wake, similar to that observed in the unstratified case. The disorder of the wake structure in the vertical increases with increasing F, and at $F = 64$ (figure 6) the wake very rapidly occupies the entire observation window. The higher F values are reached partly through smaller D, so the difference in z/D is considerable. Tilted structures with longer coherence in x than in z can be seen in all cases. Even at $F = 64$, the disturbances eventually settle to give a smaller number of larger-scale structures that appear to diffuse slowly without further rapid changes of shape.

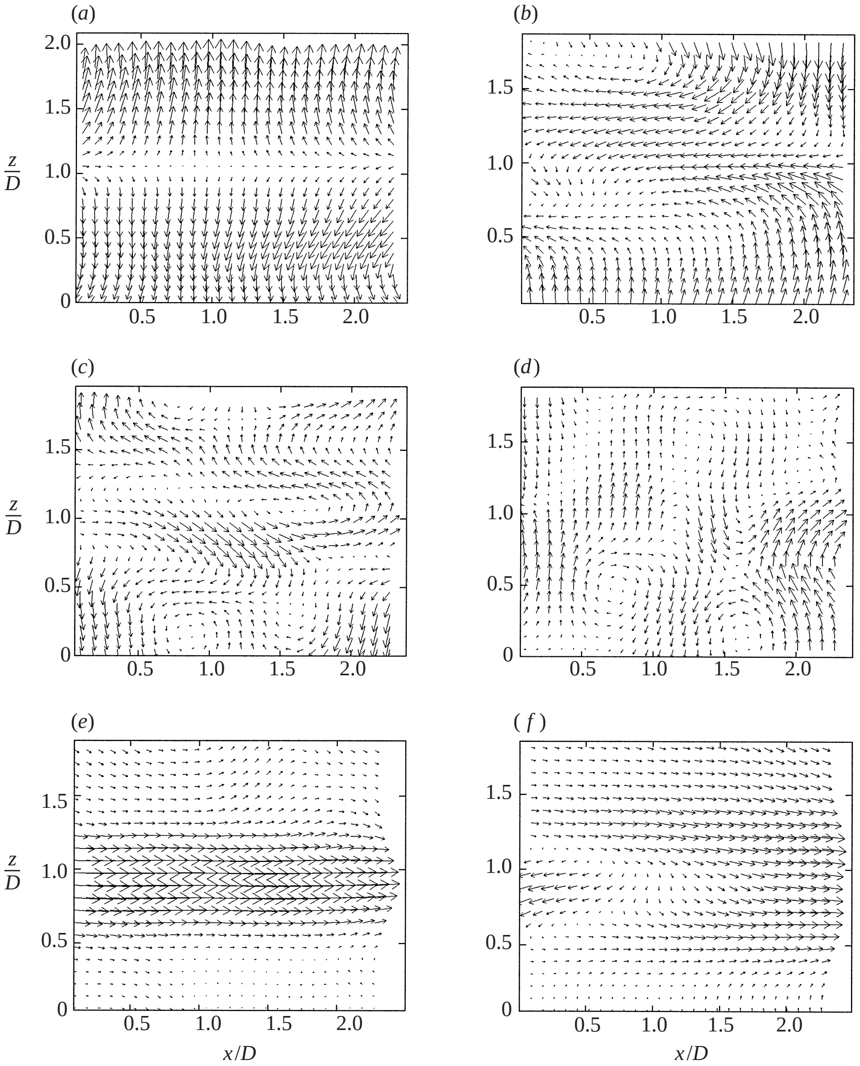

FIGURE 4. $\{u, w\}(x, z)$ for $F = 4$ and $y/D = 3.5$ at $Nt = [22, 41, 64, 92, 128, 171]$ in (*a*)–(*f*). The vector length shown is 8 times the original mean particle displacement, which increased as a power law calculated from initial experiments. Every second vector is omitted for clarity.

The peak vorticity magnitudes (also the colour bar scaling in figures 3, 5 and 6) shown in figure 7 show a rather uniform power law decay at $y/D = 0$ for all F, but the behaviour at $y/D = 1$ and 3.5 varies with F. At $F = 4$, the wake is more compact in y, so off-centreline slices pick up the wake scaling at later Nt than at $F = 16$, 64. At $F = 64$, the entire measurable wake almost immediately scales as the centreline does.

The magnitude of $|\omega_y|_{max}/(U/D)$ decreases with increasing F. In SBF96, the vertical vorticity magnitude could be rescaled by noting that as $U_0/U \sim (x/D)^{-2/3}$, and $L_H/D \sim (x/D)^{1/3}$, so

$$\frac{|\omega_z|}{(U/D)} \sim \left(\frac{x}{D}\right)^{-1},$$

(a) $y/D = 0$

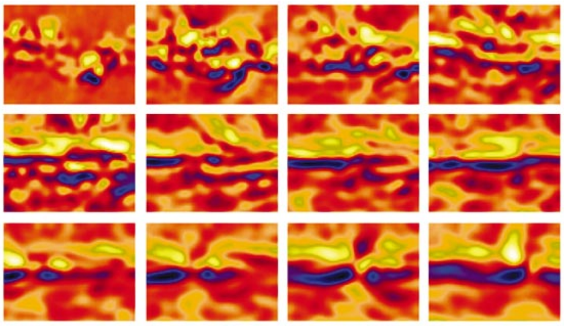

(b) $y/D = 1$

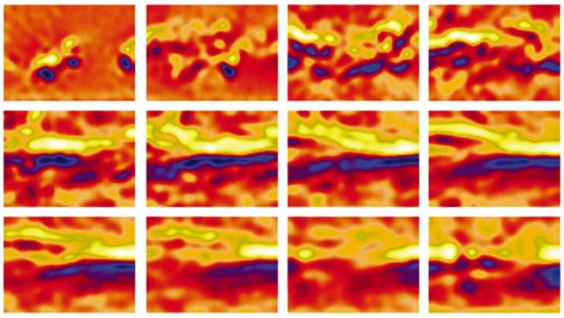

(c) $y/D = 3.5$

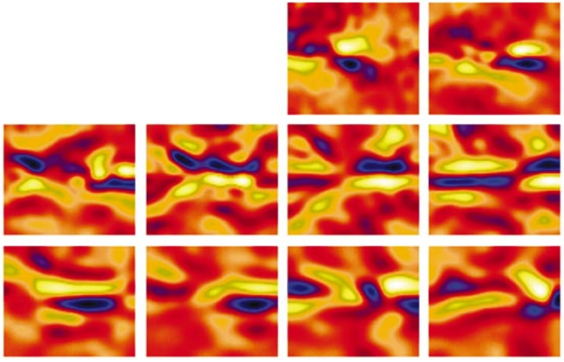

FIGURE 5. $\omega_y(x, z, Nt)$ for $F = 16$ and $y/D = \{0, 1, 3.5\}$. $Nt = \{3, 7, 10, 14, 19, 24, 30, 36, 43, 51, 59, 69\}$ and $[\Delta X/D, \Delta Z/D] = [4.40, 3.22]$, $[4.32, 3.00]$, $[3.85, 3.09]$. Qualitative details as in figure 3 caption.

and

$$\frac{|\omega_z|}{(U/D)} F \sim (Nt)^{-1}.$$

A similar scaling of ω_y (figure 8) is moderately successful in collapsing the figure 7 data. There is no physical argument to justify the use of a scaling for L_V borrowed from L_H, but it is useful for comparison. The uniform decay rate in $\omega_y \sim Nt^{-1}$ throughout NEQ and the initial Q2D phases does not mirror the segmented pattern of other quantities such as U_0, and so the discontinuous kinetic energy decay rates, by implication, are due more to systematic rearrangements of vortex lines, rather than any abrupt changes in diffusion of vorticity. Although the decay rate is superficially similar to that of the vertical vorticity (ω_z), it is actually lower, and the absolute (*a*) $y/D = 0$

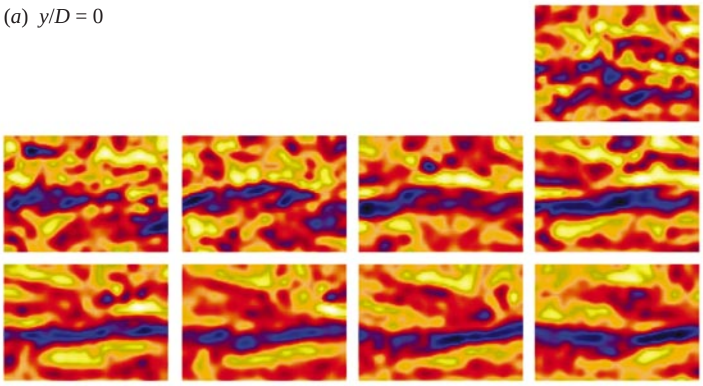

(*b*) $y/D = 1$

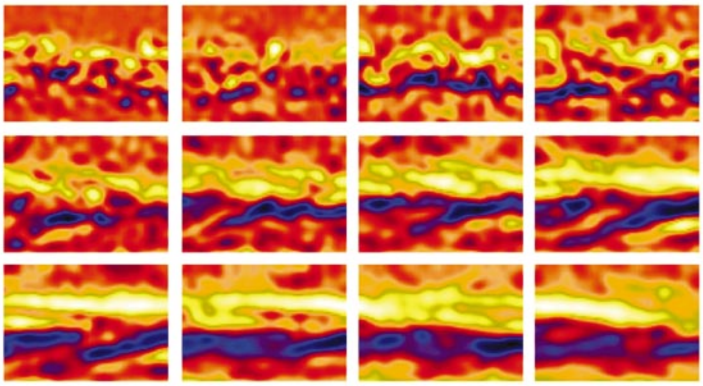

(*c*) $y/D = 3.5$

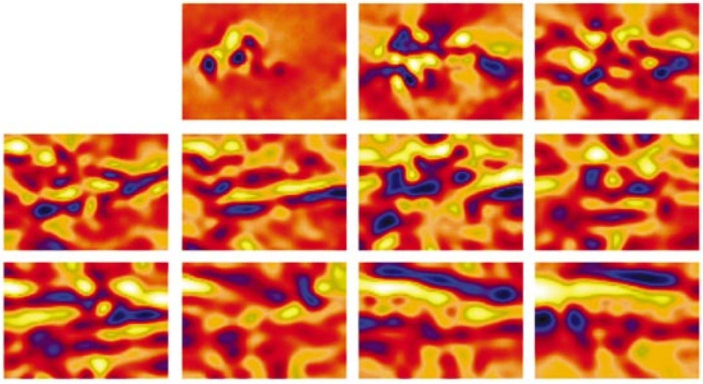

FIGURE 6. $\omega_y(x, z, Nt)$ for $F = 64$ and $y/D = \{0, 1, 3.5\}$. $Nt = \{2, 5, 9, 13, 17, 22, 28, 34, 41, 48, 56, 66\}$ and $[\Delta X/D, \Delta Z/D] = [6.00, 4.08]$, $[5.77, 3.92]$, $[5.45, 3.72]$.

magnitude is higher at any given Nt. Data in SBF96 do not extend down to such early Nt, but at $Nt = 100$, $[|\omega_z|_{max}/(U/D)]F \simeq 0.2$–$0.3$ for $1 \leqslant F \leqslant 8$, and the solid diagonal line in figure 8 is extrapolated in the middle of this range. In figure 8, $[|\omega_y|_{max}/(U/D)]F \simeq 0.5$–$0.6$ for $4 \leqslant F \leqslant 64$. The F ranges differ, but in neither separate range is there any significant residual F-dependence. Thus, $|\omega_y|$ is about 2–3 times $|\omega_z|$, consistent with the measured aspect ratios in § 4.2.2.

Although the large-scale, primarily horizontal motion induced by the vertical vorticity in the pancake eddies is the most prominent feature observable in the

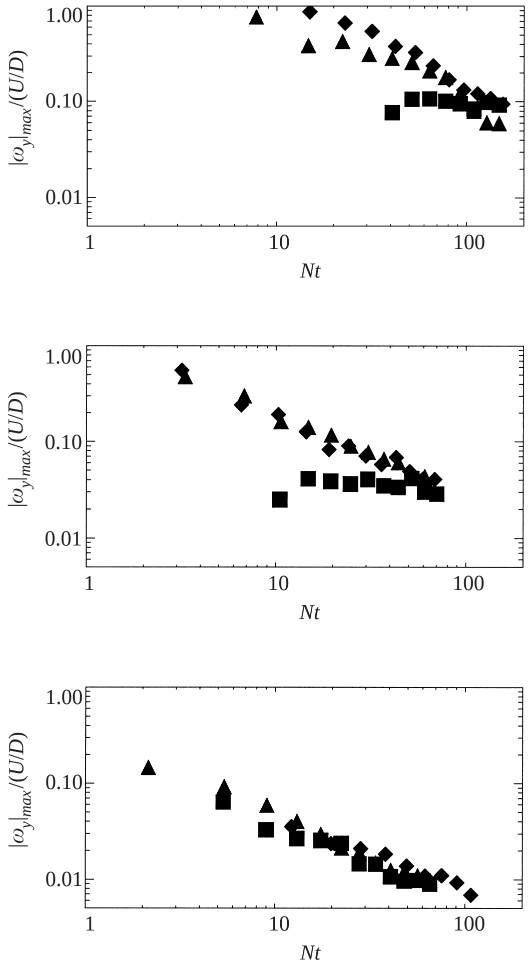

FIGURE 7. Normalized $|\omega_y|_{max}(Nt)$ for $F = \{4, 16, 64\}$ in (*a*), (*b*) and (*c*). The individual data points correspond to the numerical scaling of the colour bar in figures 3, 5 and 6. $y/D = \{0, 1, 3.5\}$ for symbols {◆, ▲, ■}.

laboratory, it is the horizontal vorticity in the vertical variation in these motions and at the upper and lower wake boundaries that is most intense, echoing at least qualitatively the findings of Fincham *et al.* (1996) for stratified grid turbulence.

4.1.2. *Mean flow*

The vertical wake scale and streamwise-averaged velocity at the centreline are plotted for a range of Froude numbers in figure 9(*a*, *b*). Since larger Froude numbers are generally achieved by using smaller spheres, the equivalent downstream distance, x/D, of the measurements increases also. The control experiments without stratification (filled squares) evolve as

$$\frac{L_V}{D} \simeq 0.3\left(\frac{x}{D}\right)^{0.34}, \tag{4.1}$$

and

$$\frac{U_0}{U} \simeq 0.5\left(\frac{x}{D}\right)^{-0.85}. \tag{4.2}$$

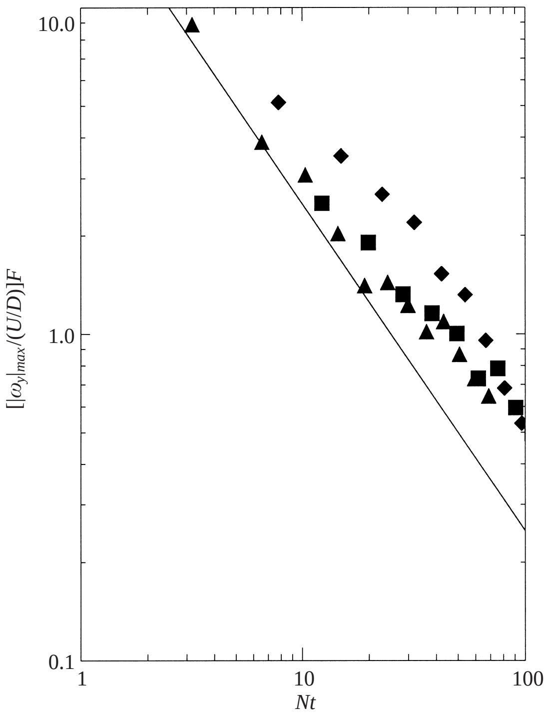

FIGURE 8. Rescaled $|\omega_y|_{max}(Nt)$ for $F = \{4, 16, 64\}$ from the previous figure, for $y/D = \{0\}$. The leading diagonal is for $|\omega_y|_{max}/(U/D) \sim (NtF)^{-1}$, from SBF96.

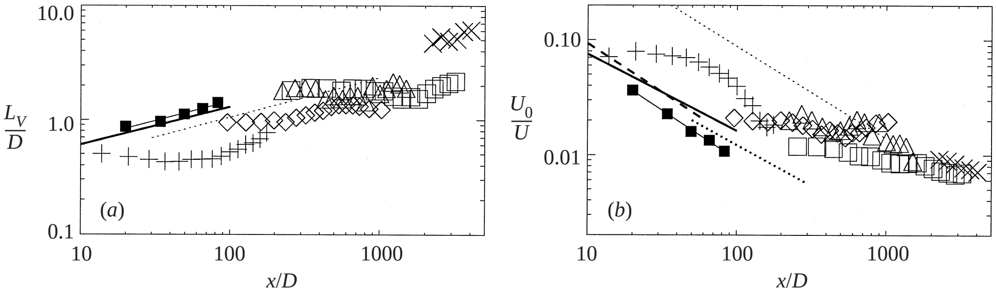

FIGURE 9. The evolution of wake height (*a*) and mean centreline velocity (*b*) for $F = \{4, 16, 57, 128, 512\}$, symbols $\{+, \diamond, \triangle, \square, \times\}$. The light dotted lines are mean power-law fits to data published in SBF96 and Sp97 for horizontal centreplane slices. The heavier lines are for unstratified wakes: ——, Bevilaqua & Lykoudis (1978); - - -, Gibson *et al.* (1968); · · ·, Uberoi & Freymuth (1970). The filled squares are unstratified data from the current experiments.

The power-law exponents do not differ significantly from the literature results (also shown). The streamwise-averaged vertical extent of the stratified wakes does not grow in a simple power law, and the wake profiles themselves differ significantly from the Gaussian cross-section of the horizontal profiles. At each Froude number, the initial wake thickness remains approximately constant up to an x/D that increases with F, equivalent to $Nt \approx 40$–80. The flat initial curves are consistent with the latter parts of the curves in figure 7 of Lin & Pao (1979) for self-propelled, slender bodies.

Once initially turbulent motions have extended vertically into the ambient, they remain active across this domain of weakly mixed fluid (mixing is weak in the sense that subsequent restratification can and does occur). Roughly speaking, this period corresponds to the NEQ régime, and to the top two rows of figures 3, 5 and 6. Note that the initial values correspond closely to the unstratified data, and hence to the horizontal length scales previously reported for the stratified wakes.

The $U_0/U(x/D)$ curves should be identical for both vertical and horizontal cuts through the (same) centreline. For all F (more than two orders of magnitude in range), the data points begin at the three-dimensional, unstratified result, and then approach the horizontal, stratified wakes result shown by the upper dotted line in figure 9. The significantly lower energy decay rates during this time are consistent with those given in Sp97. Each set of symbols marks one single experiment, and the data are much less regular than the original findings for the horizontal centreplane. Here, there is no natural confinement of the flow in the plane normal to the light slice, and the wakes are neither perfectly straight, nor perfectly aligned with the light sheet. As the wake meanders through the observation plane, even field-averaged quantities can fluctuate significantly. The difficulty is particularly acute at $F = 4$, where, as will later be shown, the wake is much more compact than in higher-F cases.

The average structure in the y-direction can be constructed from the $F = \{4, 16, 64\}$, $y/D = \{0, 1, 3.5\}$ series in figure 10, where L_V/D and U_0/U are plotted as functions of Nt, normalized by powers of F that would give the appropriate scaling in x/D, as explained further in SBF96. The three rows of figure 10 show the three different y/D locations. In previous horizontal-plane experiments, these scalings successfully collapsed the data for $F \in [2, 240]$, but they clearly do not for L_V/D, where $L_V/D \sim (FNt)^{0.6}$ is a more successful, but purely empirical, result. There is a further F-dependence in the initial wake height, which also scales approximately as $F^{0.6}$. The F-dependence is maintained at least up until $Nt \approx 100$. When $F = 64$, the data fall close to the line established for horizontal wake dimensions, which in turn was close to the unstratified result. For $Nt \geqslant 40$, vertical growth rates increase quite abruptly, with power-law exponents ranging from 0.5 to 0.3 as F increases from 4 to 64.

The accelerated late-time growth rates can be compared with the observations of Chomaz *et al.* (1993*a*), who reported much higher vertical diffusion rates in wakes at $F = 3$ and 5 than would be expected from purely viscous diffusion. They offered an explanation based on secondary vertical motions produced by Ekman layers originating at the edges of wake vortices spinning in a quiet ambient. The Ekman boundary layer thickness can be related to an eddy viscosity of a wake vortex and its initial state at some characteristic time, $Nt_0 = 100$, in which case a vertical diffusion time relative to the viscous diffusion time was found to scale as $t/t_v \sim 1/Re_0^{1/2}$, where Re_0 is based on horizontal length and velocity scales at Nt_0. Both Chomaz *et al.* (1993*a*) and SBF96 (figure 20*a*) give evidence that $Re_0 \approx 700$ for $Re = 5$ and 6.5×10^3, $F = 1$–8 and 5, respectively, when $t/t_v \sim 1/26$. The difference is in the multiplying constant, and not the power-law exponent which remains $\frac{1}{2}$. The high overall growth rates between $Nt \approx 50$ and $Nt \approx 100$, with exponents close to 0.5, the dependence of the exponent on F, and dependence of the initial height z_0 on F, and the inferred multiplying constant of 20–30 are all consistent with the results of Chomaz *et al.* (1993*a*), who further noted that neither the multilayer structure nor the dependence on F appear in their Ekman layer model. The observed faster-than-viscous vertical diffusion does not agree with the purely diffusive growth calculated and measured by Beckers *et al.* (2001) for single, low-F vortices, and this may be a qualitative difference between low- and high-F stratified flows.

In figure 10, measurements stop at $Nt \approx 100$ because the sampling criterion and L_V measurement require the mean wake profile to have a simple form (§ 3.5). This

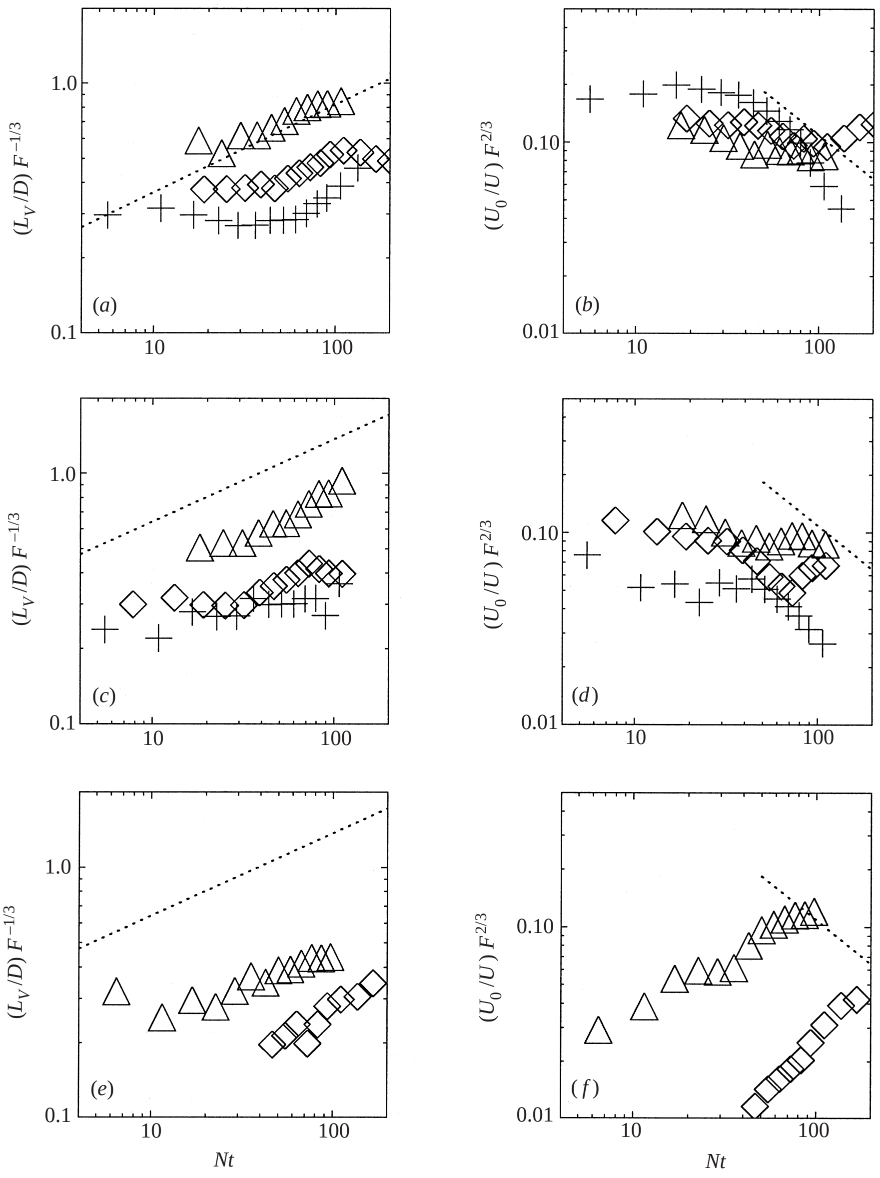

FIGURE 10. The evolution of normalized wake height (*a*, *c*, *e*) and mean centreline velocity (*b*, *d*, *f*) for $F = \{4, 16, 64\}$, symbols $\{+, \diamond, \triangle\}$ and $y/D = \{0, 1, 3.5\}$ (*a* and *b*; *c* and *d*; and *e* and *f*). The dashed lines are mean power-law fits to comparable horizontal centreplane data in SBF96 & Sp97.

terminates measurements in a conservative way, before boundary effects are likely to become important. A more thorough comparison of the various measured and predicted late-time vertical diffusion rates will require different experimental methods and facilities.

The variation in L_V/D *vs.* Nt at different y/D is seen in figure 10(*a*, *c*, *e*). The off-axis vertical length scales are smaller than at the centreline, but increase at a similar rate as the late-time centreline values, once they do start to increase. With decreasing F, the wake is more compact, and the $F = 4$ data never makes a coherent signal above the noise at $y/D = 3.5$.

The rescaled centreline velocities ought to be identical to those previously measured since the measurement is made at the line of intersection between the vertical and horizontal interrogation planes (figure 1). Figure 10(*b*, *d*, *f*) shows the mean wake defect as a function of F and y/D. In (*b*), the vertical plane data always lie beneath the dotted line established in SBF96 and Sp97, which acts as an upper bound, as already noted in figure 9.

As y/D increases, moving down the right-hand column in figure 10, the lower-F wakes have a smaller relative horizontal extent, as shown in the left-column, and the projected centreline velocity decreases also. In panel (*f*) at $y/D = 3.5$, the mean defect magnitude increases with Nt as an increasing fraction of the wake passes through the plane.

The mean wake length and velocity scales measured in vertical planes show a clear dependence on F: higher F wakes have larger initial vertical extent. The initial wake height appears to scale with $F^{0.6}$. Lower-F wakes begin as more compact, and remain so. All $F \geqslant 4$ wakes have a vertical structure that can be described as multilayered, but the layering is not as orderly as simple conceptual models allow.

The mean wake profile dominates the streamwise-averaged quantities in the wake, increasingly so as F decreases. It is useful to isolate the effect of the mean wake profile, by removing it from the velocity field data, and recalculating all quantities based on u', rather than u, as described in § 3.3.

4.2. *Fluctuating quantities*

4.2.1. *The structure of* $\omega_y'(x,z)$ *for* $F = 4, 16, 64$

Figure 11(*a*, *b*, *c*) can be compared with figures 3(*a*), 5(*a*) and 6(*a*). The differences between the total and fluctuating vorticity distributions, predictably, are greater at $F = 4$, as soon as the mean profile becomes established there.

The discernible patterns inside what will be classified as the wake region, are multiple-layered patches having greater extent in the streamwise direction than in the vertical. These slabs of ω_y' make a small angle with the horizontal, which decreases with time – the same tilt angle noted particularly in figure 3(*b*). The mean tilt of the thin shear layers can be interpreted as a stretching of an initially isotropic vorticity field (waves and vortices alike) by the mean wake profile. High-speed fluid at the centreline advects vortex lines further in x here than at the periphery. Consequently, the mean angle of inclination, β, may be simply related to a characteristic vertical wake height, L_V, and the mean centreline velocity, U_0, as

$$\beta \sim \arctan \frac{L_V}{U_0 t}. \tag{4.3}$$

One can define a local Froude number, $F_U = U_0/NL_V$, where F_U is the ratio of horizontal wake inertia to the vertical restoring force. It is like an integral wake aspect ratio with value increasing in time, and it sets the tilt angle as

$$\beta \sim \arctan(NtF_U)^{-1}. \tag{4.4}$$

Later, we will show that $L_V \sim F^{2/3}$, and since it is also known (SBF96) that $U_0 \sim F^{-2/3}$, then at any fixed Nt, (4.4) predicts

$$\beta \sim F^{-4/3}. \tag{4.5}$$

The pancake inclination angle, β, should decrease with time, and with increasing initial F. Interestingly, the rotation of a tilted vortex can provide a simple physical mechanism for late-wake internal wave generation. This topic will be pursued in detail elsewhere.

The distribution of $\omega'_y(x, z)$ at $y/D = 0$ is moderately complex for all $F \geqslant 4$ studied here. All cases show evidence of vertical layering, even if the layer geometry is not simple. Remembering that D decreases from 5.08 to 2.54 to 1.90 cm in figure 11 as F increases from 4 to 64, characteristic vertical scales, or layer heights, normalized by D will increase significantly with F (as did L_V, figure 9). If $F = 4$ is indeed a minimum for complex vertical structure to occur, then the prediction in SBF96 that the number of layers per unit diameter must be a maximum at $F = 4$ is supported.

Certain of the cartoon objects in figure 2 can be identified in the complex real flow, but they are embedded in numerous other, less readily recognizable patterns.

4.2.2. *Local length and velocity scales*

Figure 12 shows the ratio of mean-square velocity fluctuations in the vertical and horizontal directions, (*a*) including and (*b*) excluding contributions from the mean wake profile. From the time when measurements are possible ($Nt \geqslant 3$), $\langle w^2 \rangle < 0.1 \langle u^2 \rangle$, and the ratio decreases steeply with Nt, with power-law exponents ranging from -1.6 for $F = 4$ to -1.1 for $F = 64$. The Froude number dependence is removed when the mean profile is removed (figure 12*b*) where, until $Nt \approx 20$, the ratio of $\langle w^2 \rangle / \langle u'^2 \rangle$ is close to 1. After this point, the ratio declines, i.e. vertical velocity fluctuations decline more rapidly than horizontal ones, a rather well-known result in stratified grid turbulence experiments (e.g. Liu *et al.* 1987; Thoroddsen & Van Atta 1993).

Mean and individual heights of flow structures can be estimated from single vertical transects. Any single vertical line or plane survey will systematically underestimate the maximum vertical dimension of an object that is not uniform in the normal direction. Statistical corrections for this bias can be applied if the three-dimensional shape is known. However, if we suppose a vertically stacked array of arbitrarily shaped structures, and if the individual shape and fluctuation amplitude are ignored, then average fluctuation wavelengths can be used to estimate vertical patch length scales. Sub-sampling the data in this fashion is analagous to making single instrument drops in ocean surveys, with many, but not all of the attendant limitations. An example is shown in figure 13, which also compares ω'_y and $\partial u'/\partial z$ alone. A single profile is shown at four timesteps for $F = 4$. The profile location is fixed and the wake is allowed to move past it; $\partial u'/\partial z$ (dotted line) is an accurate measure of the location and spacing of fluctuations in ω'_y, but for $Nt < 10$, the amplitude can be incorrect by factors of two or more (figure 13*a*). This implies a significant correlation of $\partial w/\partial x$. For $Nt > 30$ (figure 13*c, d*), the difference is usually less than 10%. It is not uncommon for the apparent number of peaks in the $\omega'_y(z)$ curve to increase slightly at intermediate times. One may also note the temporary, large decrease in amplitude (from figures 13*a* to 13*c*) of the fluctuations as one structure passes through the measurement column. Later (figure 13*d*), the mean length scales and total vertical extent of the fluctuations both increase gradually with Nt.

Mean vertical length scales were calculated from average values of columnwise Fourier or wavelet (Morlet) transforms. In both cases the normalization is such that there is an implicit weighting by energy. When the raw data are ω'_y, it is by enstrophy. The mean vertical length scale, l_V, can be referred to as a layer height, and the mean number of layers in any vertical cut is $n = L_V/l_V$.

(a) $F = 4$

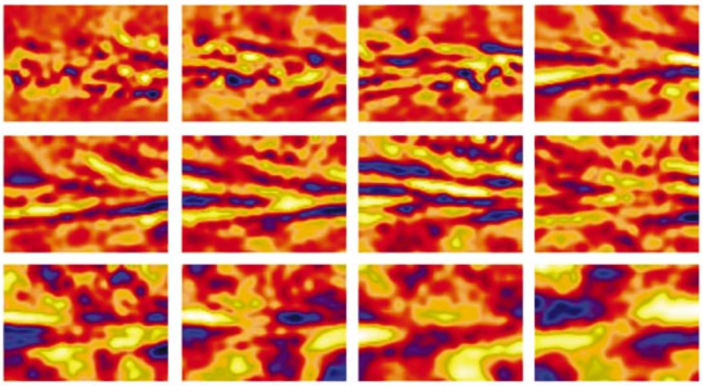

(b) $F = 16$

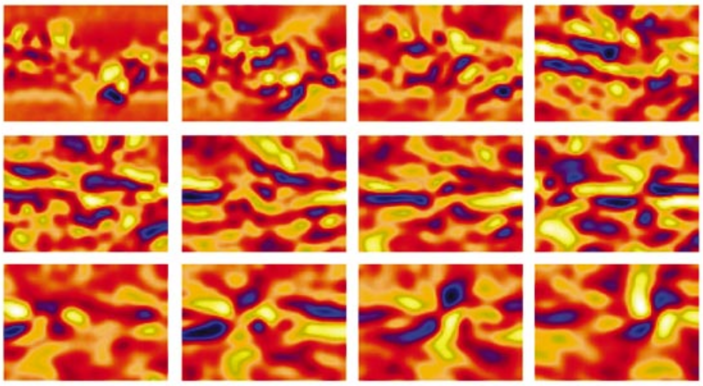

(c) $F = 64$

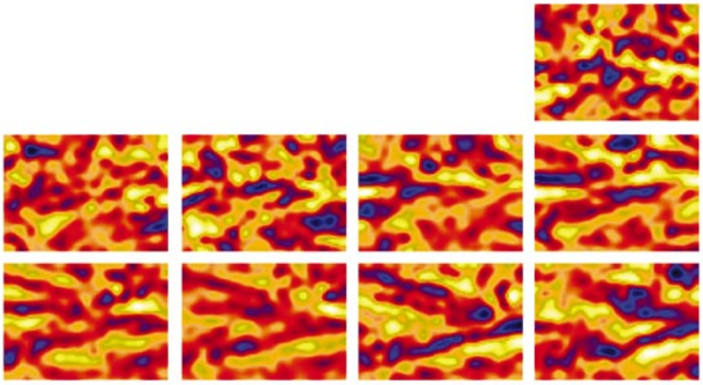

FIGURE 11. $\omega'_y(x, z, Nt)$ for $F = \{4, 16, 64\}$ and $y/D = 0$. The data are as for figures 3(a), 5(a) and 6(a), but the mean profile $U_X(z)$, and the corresponding $\partial U_X/\partial z$, has been subtracted. Note that the timesteps (given in captions to figures 3, 5 and 6) are not equal, as the average interval between frames for $F = 4$ is twice the other two cases. $[\Delta X/D, \Delta Z/D] = [2.20, 1.53], [4.40, 3.05], [6.00, 4.08]$ for $F = \{4, 16, 64\}$.

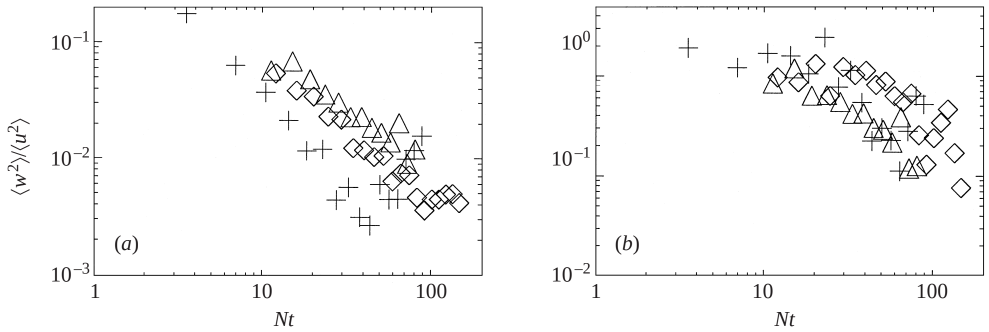

FIGURE 12. Ratio of mean-square velocities in the vertical and horizontal directions for the full flow (*a*), and for the fluctuating component alone (*b*). $F = \{4, 16, 64\}$ denoted by symbols $\{+, \diamond, \triangle\}$.

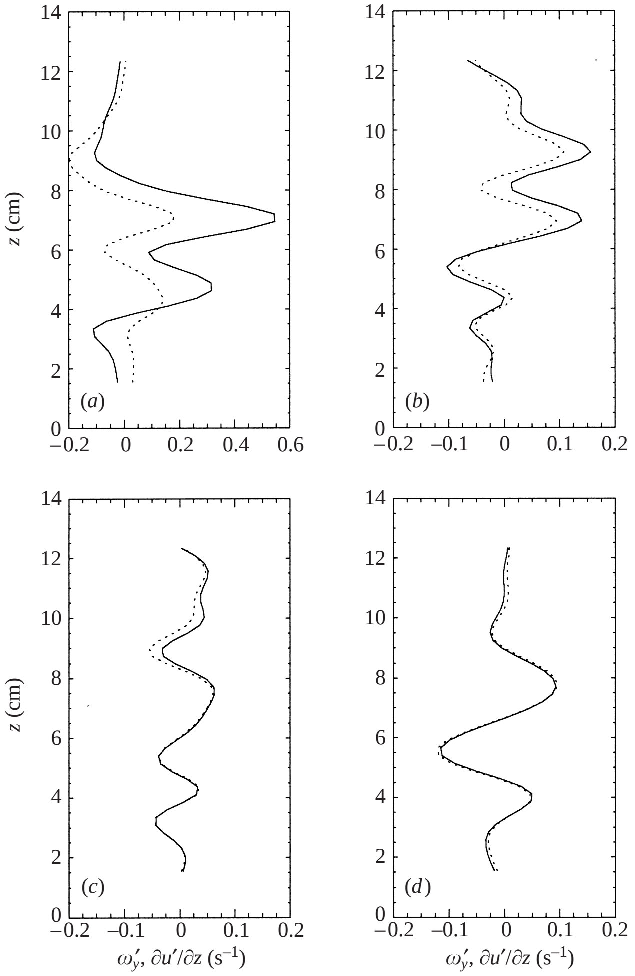

FIGURE 13. Horizontal vorticity, $\omega_y'(x, z)$ (solid line), and vertical shear, $\partial u'/\partial z$ only (dotted line), for $F = 4$, $y/D = 0$, $Nt = \{4, 18, 38, 64\}$ in (*a*)–(*d*). Neither scale is normalized and there is a scale change on the abscissa from (*a*) to (*b*).

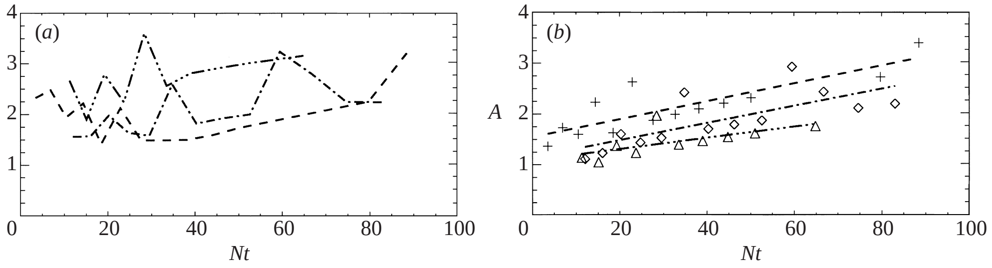

FIGURE 14. Mean number of layers in the vertical, n (a), and vortex blob aspect ratio, A (b). Data are shown for $F = \{4, 16, 64\}$ by the lines {- - - -, -·-·-·, -··········} and/or symbols $\{+, \diamond, \triangle\}$. The straight lines in (b) are linear least squares fits.

Because the vertical structure is not uniform in (x, y), the mean number of layers, n, is a difficult measurement to make (§ 3.6), further compounded by the poor wavenumber resolution at this scale. Figure 14(a) shows $n(Nt)$ and the curves show only a weak dependence on F; at $Nt \approx 50$, the end of the NEQ stage, n increases from approximately 1.5 at $F = 4$ to 3 at $F = 64$; n also varies little with Nt in the range investigated. Once the vertical extent of the wake is set, which happens early on, and does depend on F (figures 9, 10), then there is no significant reduction in layer number due to, say, merging of like-signed vortex patches in the vertical. Rather, the overall trend for n is to increase slightly after $Nt = 50$, as the layers decorrelate slowly.

The average vortex patch aspect ratio, A, is estimated from $A = l_H/l_V$, where l_H is a measure of a vortex horizontal length scale. From data in SBF96 (figure 10) and Sp97 (figure 3) an empirical scaling law fit for the evolution of the wake half-width, L_σ, can be written,

$$\left(\frac{L_\sigma}{D}\right) F^{-1/3} \simeq 0.16(Nt)^{0.35} \tag{4.6}$$

for $F \in [4, 240]$, and L_σ may be used as a measure of l_H. A cautionary remark is in order, as SBF96 found that individual vortex growth rates were slower when $Nt < 200$, as is always the case here. The consequent underestimate of l_H is not easy to quantify in a general way because the Nt ranges do not overlap, and no systematic correction is attempted. The primary effect is a likely overestimate of A for $Nt \leqslant 50$. Separate extrapolation of early and late power laws for vortex radius vs. Nt from figure 26 in SBF96 leads to a 35% increase in l_H at $Nt = 50$.

$A(Nt)$ is shown in figure 14(b). Linear least squares fits are shown through the data, primarily to clarify the systematic dependence on F, rather than implying either linear or uniform decay over the whole Nt range. Higher-F wakes have initial aspect ratios closer to 1, and continue to have lower aspect ratios up to $Nt = 80$. A increases with Nt primarily because horizontal length scales are growing faster than vertical length scales, which are almost frozen up to $Nt \approx 30$–50 (figure 9). Subsequent diffusive increase in vertical scales is counterbalanced by the decorrelation of vertical layers and concomitant increase in n. The dependence of A upon F, and final values of A between 1.6 to 3.5 are both consistent with the range of $0.2 \leqslant \alpha \leqslant 0.4$ quoted in Riley & Lelong (2000), based on their survey of existing experiments.

Having defined vertical length scales, one can define a local Froude number based

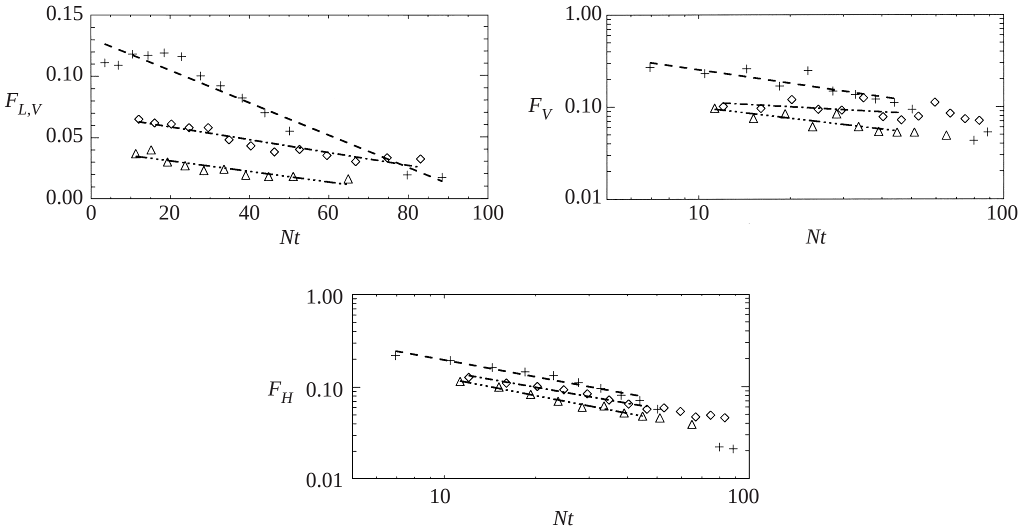

FIGURE 15. Local Froude numbers based on average wake height (*a*), average layer height (*b*), and horizontal length scale (*c*). Lines and symbols as for figure 14.

on mean wake height and local velocity magnitude, $\langle q \rangle$,

$$F_{L,V} = \frac{\langle q \rangle}{NL_V}, \tag{4.7}$$

and $F_{L,V}(Nt)$ is shown for $F = \{4, 16, 64\}$ in figure 15(*a*). There is a strong dependence on the initial F and lower-F wakes have higher local values of $F_{L,V}$. This curious result derives from the departures from horizontal scaling already observed in figure 9. From this figure, one can make the following approximate scaling arguments:

$$\frac{L_V}{D} \sim (FNt)^{2/3}, \tag{4.8}$$

and

$$\frac{q}{U} \sim (FNt)^{-2/3}, \tag{4.9}$$

in which case,

$$F_{L,V} \sim \frac{U}{ND}(FNt)^{-4/3}, \tag{4.10}$$

and $F_{L,V} \sim F^{-1/3}$. $F_{L,V}$ depends inversely on the initial Froude number because lower-F wakes have smaller vertical length scales. In figure 15(*a*), the earliest measured values of $F_{L,V}$, at $Nt \approx 5$ for $F = 4$, begin at approximately 0.12. All $F_{L,V}$ have fallen to ≈ 0.01 by $Nt \approx 100$.

A Froude number, $F_{l,V} = \langle q \rangle / Nl_v$, based on a single layer thickness should be more representative of the local dynamics, and will be denoted F_V. Since $F_V = nF_{L,V}$, and n increases slightly with F (figure 14*a*), then $F_V(Nt)$ in figure 15(*b*) shows a smaller variation with F. Eventually all values reach $F_V \leqslant 0.1$ by $Nt \approx 50$.

An equivalent Froude number based on horizontal length scales is $F_H = \langle q \rangle / NL_H$. It is related to the vertical scales by the aspect ratio, and so $F_H = F_V/A$. A is larger at lower F, and the result (figure 15*c*) is to almost collapse the data, so that F_H varies little, either in decay rate or in absolute value, with F. The independence of F_H of the initial F has been noted on at least two previous occasions. For stratified wakes, SBF96 found empirically that the scaling exponents in (4.8), (4.9) were approximately 1/3 and −2/3, respectively. Then,

$$F_H = \left(\frac{U}{ND}\right)(FNt)^{-1},$$

or $F \sim (Nt)^{-1}$ independent of F. Postulating, as usual, a constant, characteristic Nt, such as $Nt_c \approx 2$ for initial wake collapse and ignoring order-one multiplying constants in (4.8), (4.9), then $F_H(Nt_c) \approx \frac{1}{2}$. Extrapolation of the curves in figure 15(*c*) back to $Nt = 2$ gives $F_H = 0.4 \pm 0.1$. The prediction that an F-independent local turbulent Froude number of order one would develop at $Nt \approx 1$ was originally noted by Riley *et al.* (1981) (see also Riley & Lelong 2000) who showed that F-independence must follow provided a condition such as $\epsilon \sim q^3/L_H$ holds. In both cases, the F-independence is assured by either assuming or observing that length and velocity scales behave as they do in homogeneous, unstratified flows. The reasons why horizontal length and velocity scales obey such scaling laws even at late times are not clear, but given that fact, then the F-independence of those events and quantities governed by L_H follows, just as the departure from this scaling for L_V ensures that the vertical organization of the wake structure does not erase all memory of the initial F.

4.2.3. *Spatial velocity gradients*

Figure 16 shows the normalized mean-squared velocity gradients, $\langle(\partial u_i/\partial x_j)^2\rangle$, $i, j = 1, 3$. In figure 16(*a*), $\partial u/\partial x$ collapses moderately well in an envelope beneath the corresponding line for horizontal plane data. Recalling figure 1(*b*), the data ought to be the same in the two experiments, but here the averaging domain is different, including the outer region, not just the wake itself. The effect is to include propagating wave components, and to have a non-uniform averaging domain as the wake extent fills an increasing fraction over time. However, as the initial vertical wake growth rate is very low, we elect to tolerate this cost. Thus, one expects the data to fall always beneath the dotted line, as it does. The steeper decay rates are also expected, as the propagating components leave the observation box altogether.

By contrast, $\partial u/\partial z$ (figure 16*b*) does not collapse with F. In the absence of stratification, $\partial u/\partial z$ and $\partial u/\partial y$ should have similar magnitudes, and $\partial u/\partial y$ from horizontal plane measurements is shown for reference. When $F = 4$ (crosses), $\partial u/\partial z$ is mostly considerably higher than $\partial u/\partial y$. At $F = 64$ (triangles), initial values lie close to the line, but these too eventually rise above it at a later Nt. Lower-F wakes have higher contributions from the vertical gradients of the horizontal velocities.

$\partial w/\partial x$ is compared with $\partial v/\partial x$ (dotted line, figure 16*c*), which, again, might be expected to have similar magnitude in the absence of the mean density gradient. All curves lie significantly below the dotted line, showing that stratification suppresses the horizontal gradients of vertical velocity (as well as the vertical velocities themselves, figure 12), which then decay faster than they otherwise would. The magnitude of the normal strain $\partial w/\partial z$ in figure 16(*d*) is similar to the shearing term $\partial w/\partial x$. From continuity,

$$-\frac{\partial w}{\partial z} = \frac{\partial u}{\partial x} + \frac{\partial v}{\partial y};$$

its magnitude has already been used in horizontal-plane measurements as a measure of the amplitude of out-of-plane motions of the isopycnal, most of which at moderate to late times can be related to emission of internal wave packets by the unsteady wake motions.

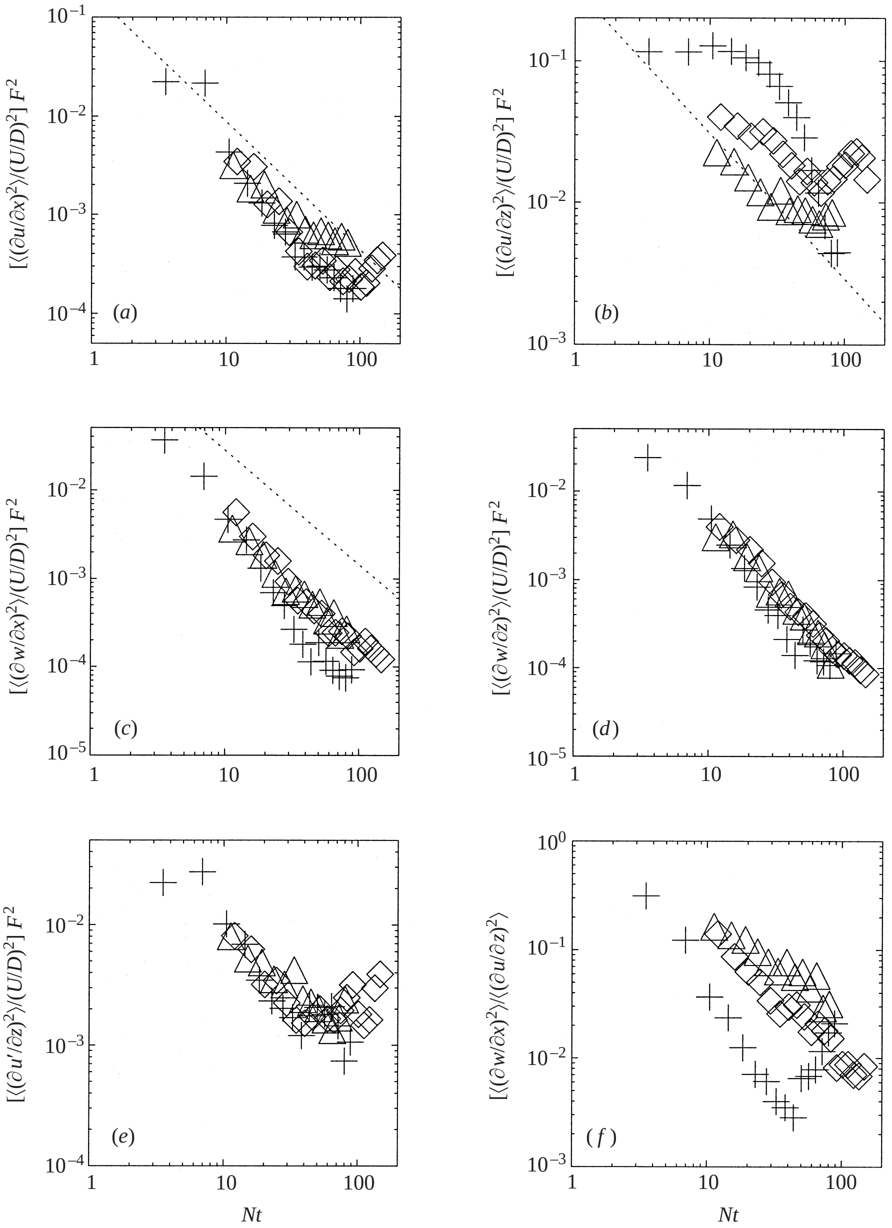

FIGURE 16. (*a*)–(*d*) The measurable mean-square velocity gradients $\langle(\partial u_i/\partial x_j)^2\rangle$, $i, j = 1, 3$. (*e*) The vertical gradient of the fluctuating component of u. (*f*) A comparison of the ratio of the two shearing terms. Where appropriate, the dotted line shows an average power-law fit to comparable horizontal plane data over $2 \leqslant F \leqslant 240$, as explained further in the text. $F = \{4, 16, 64\}$ for symbols $\{+, \diamond, \triangle\}$.

Removing the mean wake defect component of the vertical shear (figure 16*e*) shows that the remaining part now collapses with F. Finally, the ratio of horizontal shear to vertical shear (figure 16*f*) is always small. The magnitude and decay rate depend on initial F, consistent with the greater importance of the mean-flow-induced shearing motions at lower F.

Since F_V and F_H have values < 0.1 for all $Nt > 4$, all measured wake flows are buoyancy-dominated on average. Yet when vertical shearing is strong, the stability to Kelvin–Helmholtz-type overturning mechanisms could be important at small scales. A global, average Richardson number, Ri, can be defined,

$$Ri = \frac{N^2}{\langle (\partial u/\partial z)^2 \rangle}, \tag{4.11}$$

which is just 4/(figure 16*b*). Since the maximum values of the rescaled vertical shear in figure 16(*b*) are $\leqslant 0.1$, then the minimum value of $Ri \approx 40$, which greatly exceeds nominal critical values of $\frac{1}{4}$ (see Jacobitz, Sarkar & Van Atta 1997 for more sophisticated discussion on the sufficiency of the simple Ri criterion). This result echoes the findings in direct numerical simulations both by Métais & Herring (1989) and Kimura & Herring (1996) where the stratified turbulent flows were always stable (to Kelvin–Helmholtz overturns, as measured by the Ri_{min} criterion) for $N \neq 0$.

The field-averaged Ri may neglect locally unstable conditions, and a local Ri can be defined as $Ri_{loc} = N^2/(\partial u/\partial z)^2$. Figure 17 shows $Ri_{loc}(x, z)$ where $Ri_{loc} < 100$ for $F = \{4, 16, 64\}$. At all F, low Ri_{loc} values are confined to the wake centre. Contributions from shear instabilities in the far field from propagating internal waves are negligible. When $F = 4$, most low values occur at the wake edge, along the top and bottom shear layers. As F increases, the vertical variability increases, and the total area occupied by $Ri_{loc} < 100$ decreases. All cases converge in time to a smooth, plate-like configuration, whose streamwise extent decreases with F. Figure 18 shows the minimum value of Ri_{loc} over the whole field, at each timestep. All values are high, none are below $\frac{1}{4}$. Initial values have a systematic dependence on F, and most remarkably, all have an intermediate, transient drop before Ri_{loc} rises again. The magnitude of this 'hiccup' is less pronounced at higher F. It occurs some time between $Nt = 50$ and $Nt = 150$, after which, further increase in $Ri_{loc,min}$ is F-independent. This time corresponds approximately to the end of the NEQ phase, and maximum values of $\partial u/\partial z$ are achieved because there is a balance between the degree of organization of the wake, which tends to increase, and the continually decaying (on average) kinetic energy. It has previously been observed (Sp97) that the centreline kinetic energy decay rates are significantly lower during NEQ, than either before or after. As the wake structure simplifies, the onset of significant viscous losses in vertical shearing appears to coincide with the end of the NEQ régime.

Measurable components of the kinetic energy dissipation (3.8) are shown in figure 19, for the full field (*a*), and for the fluctuating part alone (*b*). S_y decreases slightly, but systematically, with F in the range $10 \leqslant Nt \leqslant 50$. Subsequently there are large variations that are most likely due to the arbitrary sampling of small numbers of large-scale structures that intersect the light sheet. S'_y also varies with F, but in the other direction, as the measured dissipation of lower-F wakes is mostly caused by the mean vertical shear of the more compact wake. The ratio of the two quantities (figure 19*c*), i.e. the fraction of the measurable dissipation components not attributable to the mean defect, depends strongly on F over a large part of the time series. Eventually, even the $F = 4$ wake loses its regular structure, and all converge at a ratio of about 0.3. The F-dependence of the vertical-plane dissipation at intermediate times is mostly attributable to the varying contribution of the mean wake profile, which is stronger at lower F, but counter-balanced in effect by the other more broadly distributed shear and normal straining regions at higher F. Before the curves begin to diverge due to sampling irregularities, the F-independence that is also observed from $Nt \approx 100$ onwards in the horizontal plane data is recovered.

(*a*) $F = 4$

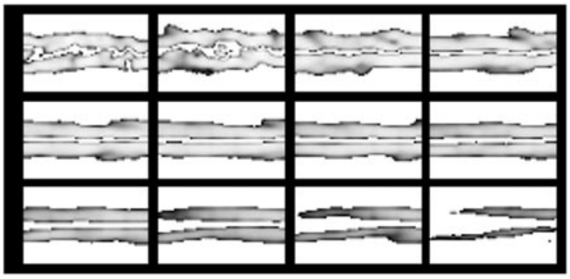

(*b*) $F = 16$

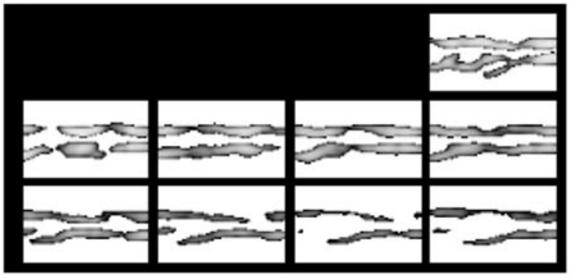

(*c*) $F = 64$

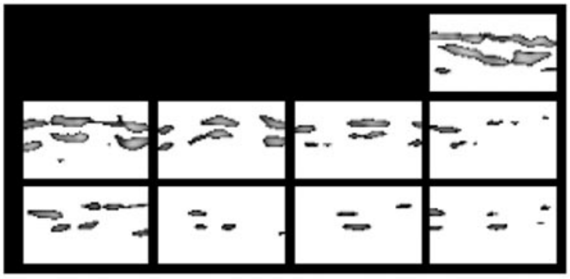

FIGURE 17. Inverted grey scale representation of the local Richardson number, for all $Ri_{loc} < 100$. Each rectangle is an instant in time, ranging from $Nt \simeq 4$ (top left) to $Nt \simeq 54$ (bottom right), and the mean flow direction is from left to right. The domain size is 20.5 × 12.3 cm.

5. Discussion

5.1. *An energy budget for the stratified wake*

Given the wake-averaged dissipation measurements in figure 19, an attempt can be made to compare them with horizontal plane contributions, and to construct an energy budget that accounts for the observed kinetic energy decay rate. In so doing, the working assumption will be that negligible mixing occurs during the observation time ($Nt \geqslant 4$), so that potential energy stored in a re-arranged density profile is ignored. Extrapolation of the mixing efficiency studies of Park, Whitehead & Gnadadeskian (1994) suggest that this is a reasonable approximation, but the initial mixing can be expected to increase with F. Conductivity probe measurements following the experiment indicate that the long-term disturbance of the mean density profile is very small, and the evidence in figure 18 supports the notion that at least during the period $4 \leqslant Nt \leqslant 150$, mixing through turbulent overturning motion is likely to be small. However, without detailed, simultaneous measurements of density profile fluctuations, the F-dependent conversion of kinetic to potential energy in

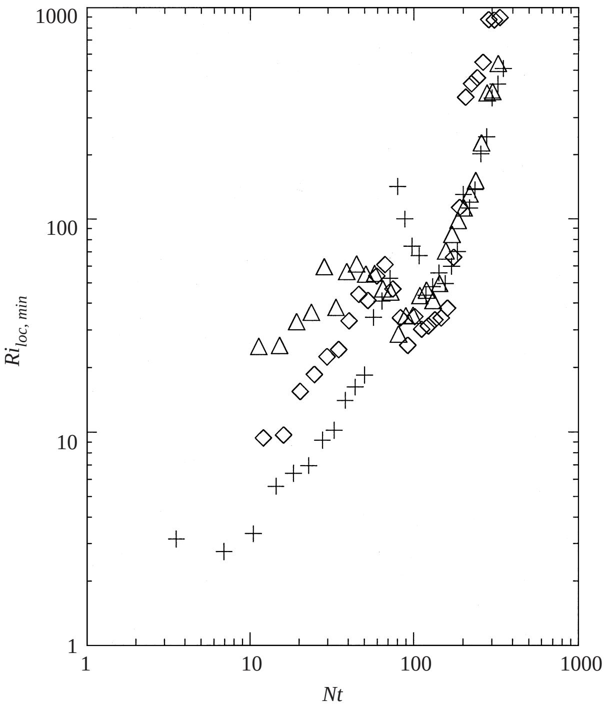

FIGURE 18. Minimum value of Ri_{loc} for $F = \{4, 16, 64\}$ for symbols $\{+, \Diamond, \triangle\}$. A local minimum occurs at $50 \leqslant Nt \leqslant 150$.

the pre-collapse, three-dimensional régime ($Nt < 2$) and its immediate aftermath ($2 \leqslant Nt \leqslant 4$) can be neither measured nor inferred.

Figure 20(*a*) is a replot of horizontal plane data from Sp97 for $F = \{10, 20, 40, 80\}$. E is the wake-averaged kinetic energy, $E = \frac{1}{2}\langle u^2 + v^2\rangle_W$. The curves can be divided into two time periods: a later time when all F curves collapse well onto a $-4/3$ line, preceded by the NEQ régime where the power-law exponent is significantly lower. The bold straight lines are least squares fits with -0.43 and -1.33 slopes, respectively. The implication is that $\epsilon = \mathrm{d}E/\mathrm{d}t$ should have a discontinuous jump at around this time, or at least a temporary rise, but none has been recorded in experiments (the unusual shape of the $Ri_{loc,min}$ curves in figure 18 is interesting in this respect).

Figure 20(*b*) combines all contributions to the measured dissipation. The top two solid lines are the mean least squares fits to measured $\dot{E}$ from the individual curves in figure 20(*a*), together with the original data in lighter curves. The notation is as part(*a*). Note the superior collapse in the late-time Q2D regime, and the discontinuity in $\dot{E}(Nt)$. The initial slope is -1.6 and the final slope is -2.33, which is equal to the $-7/3$ predicted slope from three-dimensional scaling arguments. All quantities have been averaged within the mean wake boundaries, and so dissipation rates are denoted S, to be compared with the $\dot{E}$ curves calculated from the upper part.

The thin solid line running diagonally from top left to bottom right of the graph is S_z from coefficients given in SBF96, table 3, for $F \in [1.2, 10]$. It is lower in magnitude, and has different slope (-1.83) than the observed $\dot{E}$. It is also extrapolated back to much smaller Nt than was measured in these original experiments ($Nt_{min} \approx 20$), and so must be treated as somewhat speculative. The mean S_z from data in Sp97 for $F = \{10, 20, 40\}$ are plotted as a single dashed line. It too has characteristics

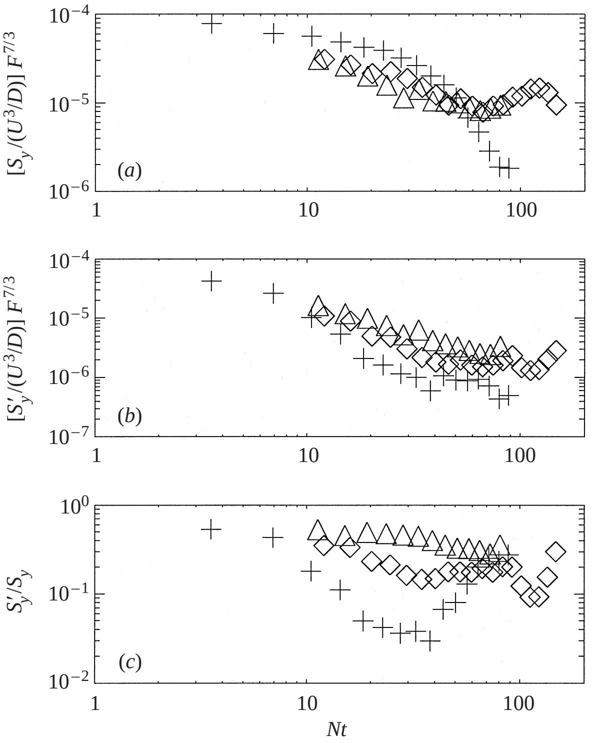

FIGURE 19. Total contributions of in-plane velocity gradients to the kinetic energy dissipation, for the unmodified flow (*a*), for the fluctuating part alone (*b*), and their ratio, (*c*), for $F = \{4, 16, 64\}$, symbols $\{+, \Diamond, \triangle\}$.

that differ from the observed $\dot{E}$ line(s) (slope is -1.70), but does not differ beyond experimental uncertainty from the continuous line. It is worth noting that the lower slopes are quite similar to the early observed energy decay rates, not the final ones. These data in figure 20 can be compared and/or combined with the dissipation rates from the vertical slice data, calculated as follows.

Dissipation ϵ_y was calculated from (3.8) and averaged over the wake height to yield S_y. It is assumed that isotropy in the horizontal plane is broken only by the mean wake profile, and so $S_y' \approx S_x$. Hence S_W, the total wake-averaged dissipation rate, is calculated from

$$S_W = S_z + S_y + S_y' - 2\nu\left[\overline{\left(\frac{\partial u}{\partial x}\right)^2} + \overline{\left(\frac{\partial v}{\partial y}\right)^2} + \overline{\left(\frac{\partial w}{\partial z}\right)^2}\right], \qquad (5.1)$$

where the last term in square brackets comes from the fact that each pair of orthogonal measurement planes has one normal strain component in common, as described in figure 1. Recall that (3.8) was defined for convenience as a positive quantity, from which the extra normal strain counts must be removed. Equation (5.1) can also be written

$$S_W = S_y + S_y' + \nu\left[\overline{\left(\frac{\partial u}{\partial y}\right)^2} + \overline{\left(\frac{\partial v}{\partial x}\right)^2} + 2\overline{\left(\frac{\partial u}{\partial y}\frac{\partial v}{\partial x}\right)} - 2\overline{\left(\frac{\partial w}{\partial z}\right)^2}\right] \qquad (5.2)$$

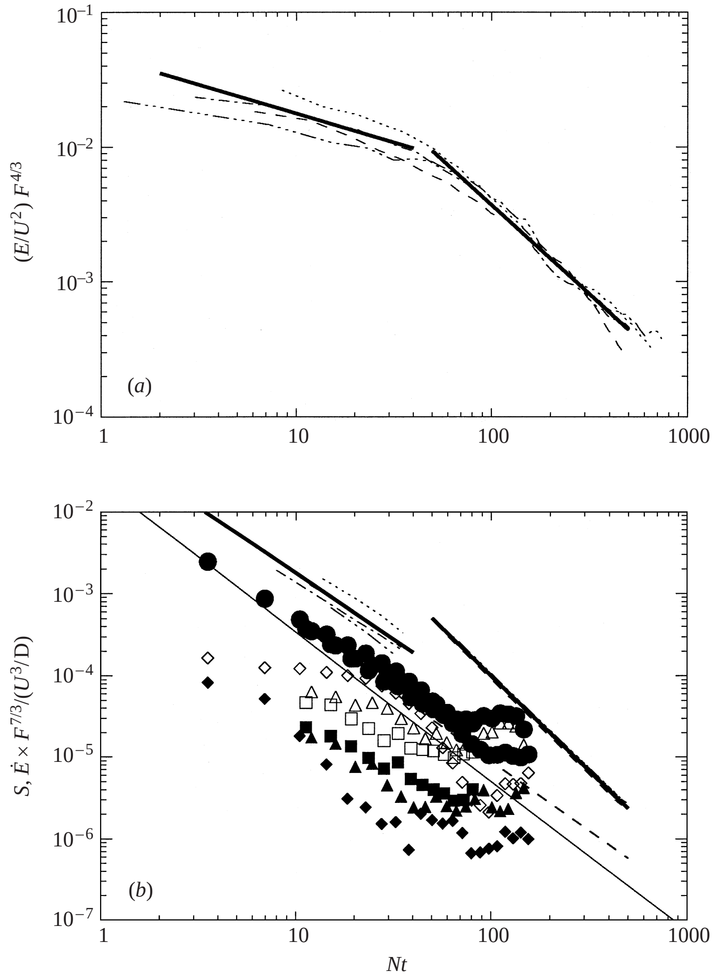

FIGURE 20. (*a*) The decay of normalized, wake-averaged kinetic energy from experiments in Sp97 for $F = \{10, 20, 40, 80\}$ in light lines {· · · ·, - - - -, -·-·-·, -· · · -· · · -· · ·}. The heavy solid lines are least squares fits through these data. The mean slopes provide the two solid lines near the top of (*b*), which combines estimates of the kinetic energy dissipation rate $(S, \dot{E})$ from several sources. The single solid line running from top left to bottom right is a mean curve for horizontal-plane dissipation rate measurements (S_z) in SBF96 for $F \in [1.2, 10]$. The dashed line (mostly obscured) is the same measurement from Sp97 for $F = \{10, 20, 40\}$. The open and closed symbols come from experiments described in this paper (figure 19) for $F = \{4, 16, 64\}$ shown as {◇, △, □} respectively. Open symbols are S_y and closed equivalents are $S_y' \approx S_x$, as described in the text. S_W, the total measured dissipation is calculated from the sum of S_y, S_y' and S_z as in (5.1) and is shown by solid circles. These can be compared with the original solid lines at the top of the figure.

when all the terms in the square brackets can be calculated from horizontal-plane measurements, while S_y and S_y' come from the vertical plane.

S_y and S_y' are shown in figure 20(*b*) as open and closed symbols, respectively, for $F = \{4, 16, 64\}$. Thus the lower, filled diamonds are S_y' for $F = 4$, and the upper, open diamonds are S_y for the same case. Because the lower-F case is more strongly influenced by the mean wake profile, the relative contribution to the dissipation from the fluctuating components increases with F. The S_y' is always lower than S_y, but at $F = 64$ the difference is much smaller than at $F = 4$.

The S_y and S_y' data points for the calculated vertical-plane dissipation rates lie at first beneath the solid line for the mean horizontal plane measurements. This may be deceptive, because the horizontal-plane measurements do not necessarily extrapolate back to $Nt \leqslant 20$, and the lower slopes of the initial $\dot{E}$ curves from the same origin in figure 20(*a*) could be interpreted to imply just this. On the other hand, fluid motions in the vertical can generate propagating wave modes with low associated dissipation rates. Internal waves remove energy from the local wake region, but not primarily by viscous dissipation. Energy transferred to wave modes is not available for the usual cascade-type mechanisms to small dissipative scales. At the same time, the high values of $Ri_{loc}(x, z)$ and $R_{loc,min}$ (shown in figures 17, 18) suggest that shear instabilities themselves, either inside or outside the wake region itself, are very unlikely to play a significant rôle during this period, which is early in the experiments, but still comparatively late with respect to number of buoyancy periods elapsed.

For $Nt \approx 10$–50, the slope of S_y and S_y' *vs.* Nt is significantly lower than S_z, and all the S_y components eventually cross the S_z curve. As they do, their decline with increasing Nt is very low, and the result is to move the measurements up to the higher, late-time dissipation rates measured from $\dot{E}$. At all F, the largest velocity gradients in the vertical plane beyond $Nt \approx 10$ are the vertical gradients of horizontal velocity ($\partial u/\partial z$ in figure 16*b*), and with increasing Nt it is this component that comes to dominate the S_y measurement. At $Nt \approx 20$, S_y is comparable in magnitude to S_z. At moderate to late times, $Nt \geqslant 100$, the vertical growth and energy dissipation are controlled primarily by viscosity. The layers slowly continue to decorrelate in the vertical, and the vertical shearing between them is mostly responsible for the kinetic energy dissipation. S_y now becomes a factor of 2–8 times S_x (the possible sampling errors make it impracticable to make this estimate with less uncertainty from single vertical slices).

The net result, S_W, is shown as solid circles in figure 20(*b*) and is F-independent. S_W always lies beneath $\dot{E}$, suggesting that the energy budget is incomplete. The calculation of S_W from (5.1) assumes both that the simplification of (3.8) is justified over the averaging operation, and also that cross-straining terms that cannot be cross-calculated between separate experiments are similarly small. However, this omission in calculation is likely to be dwarfed by the almost complete omission of the kinetic energy of the internal waves generated by the wake itself. The wake averaging procedure ignores all far-field motions, and hence propagating wave modes, even those that remain intersecting the plane of observation. Figures 3–6 have demonstrated qualitatively the co-existence of propagating, periodic motions, and their generation by comparatively late-time (NEQ) wakes has been previously reported by Gilreath & Brandt (1985), Bonneton *et al.* (1993, 1996) and Spedding (1999) and Spedding *et al.* (2000). More detailed quantitative experiments are in progress.

An interesting part of the result is the levelling off of the solid circles, which appear to approach the late-time decay measured in horizontal centreplanes. A levelling of the decay rate in S signals the beginning of the vertical shear taking over primary importance in the energy dissipation, and it occurs early in the Q2D phase, $Nt > 70$, when averaged quantities involving w can be ignored (figures 12, 13). Clearly S_y now assumes the dominant rôle, but the factor of 2–8 is somewhat smaller than the 90% found by Fincham *et al.* (1996), a result which appeared at Nt as early as 20. There are two significant differences between the experiments: first, the grid turbulence was generated with a rake of vertical bars in a deliberate attempt to minimize the generation of internal waves. The initial forcing is therefore two-dimensional, with the initial vorticity vectors aligned parallel to the rake bars and to the gravity vector, and the state of very low w is reached much sooner than if the original forcing, such as over a three-dimensional obstacle like a sphere, were to generate significant w velocities. The second difference comes from the fact that the wake is a localized turbulent source, free to expand (by entrainment, vortex merging, diffusion, wave generation) in y and z. Grid turbulence filling a density-stratified box has no such option, where the sea of densely packed vortex blobs must continue to interact strongly with neighbours on all sides without the possibility of escape. Ultimately, we arrive at the perennial problem of stratified flow investigations, where initial conditions affect the long-time structure and dynamics (as illustrated famously in the numerical simulations of Métais & Herring 1989). If the objective is to model intermittent ocean or atmospheric turbulence events, then the magnitude of vertical shear may be overestimated by turbulence-in-a-closed-box simulations.

5.2. *What determines the vertical length scale?*

If the Osmidov overturning length scale argument of § 1.4 is applied to the sphere wake by assigning length and velocity scales according to their initial values immediately behind the sphere, $l \sim D$, $u \sim U$, equation (1.6) for l_o scales as

$$\frac{l_o}{D} \sim F^{3/2}. \tag{5.3}$$

If a mean or maximum vertical length scale is related to l_o, then it increases with F for fixed D.

A refinement of this argument takes into consideration the early time evolution of u and l up to a presumed moment of collapse where the vertical scale is set. Thus, at early times, $l < l_o$, and if the turbulence is assumed not to feel the effects of stratification, length and velocity scales evolve as they would in a homogeneous fluid (a reasonable inference from the data for a wide range of F in figure 9). Expressing the result in terms of Nt,

$$\frac{l}{D} \sim (FNt)^{1/3}, \quad \frac{u}{U} \sim (FNt)^{-2/3}. \tag{5.4}$$

If Nt_c is approximately a constant, then, substituting (5.4) into (1.6) gives

$$l_o = \left(\frac{F^{-7/3}U^3}{DN^3}\right)^{1/2}, \tag{5.5}$$

a result which could also have been obtained directly from the observed $F^{-7/3}$ scaling of the kinetic energy dissipation rate. Consequently,

$$\frac{l_o}{D} \sim F^{1/3}. \tag{5.6}$$

A layer height set by l_o at Nt_c increases with F. The value of the scaling exponent depends on the assumptions made about the intermediate, pre-collapse decay rates (cf. (5.3), (5.4)), but it is always positive. Empirical estimates of the multiplying constants allows the absolute layer height and its variation with F to be predicted. Moreover, if multiple layer formation requires a minimum value of F, such as $F_{ml} \geqslant 4$, then (5.6) also predicts that F_{ml} corresponds to the value of F at which the number of layers per unit diameter is a maximum.

Arguments of this kind are most clearly applicable to initially homogeneous turbulence that decays either with time and/or distance from its source, such as grid turbulence in laboratory experiments or numerical simulations with broadband initial conditions. However, linear instability mechanisms have also been discovered in rotating and/or stratified flows that can be responsible for decoupling or decorrelating initially vertically coherent structures. Indeed, in the late-time evolution of stratified flows, the most evident process is decorrelation of vertical layers (see also, for example, the laboratory experiments of Chomaz *et al.* 1993*a* and Fincham *et al.* 1996, and numerical simulations of McWilliams, Weiss & Yavneh 1994, Dritschel & de la Torre Juárez 1996 and Dritschel, de la Torre Juárez & Ambaum 1999). Over the time interval $50 \leqslant Nt \leqslant 100$, the small increase in the layer count, n (figure 14*a*) and the concomitant decrease in $Ri_{loc,min}$ (figure 18) is consistent with a gradual decorrelation of layers in the wake experiments reported here. The possible mechanisms will briefly be surveyed before assessing their likely influence together with the local length-scale-type arguments outlined above.

The theoretical stability of initially columnar vortices in a stratified fluid has been considered from three widely differing viewpoints. Dritschel & de la Torre Juárez (1996) examined the linear stability of an elliptic vortex in the quasi-geostrophic equations to three-dimensional disturbances as a series of small two-dimensional displacements. In the freely rotating case (i.e. without an external straining field), the most amplified mode is a long-wavelength twisting of the vortex column, whose growth rate depends only on the height-to-width aspect ratio, provided the column is tall compared with f/N, where f is the Coriolis parameter. Although the instability mechanism is quite general, the particular case of stratified wakes has no opportunity to develop long-wavelength instabilities of this kind because such tall, slender columns are not formed in the first place. By the time the flow becomes sufficiently two-dimensional that one may set $w \approx 0$, the scale selection has already occurred.

A combined experimental, theoretical and numerical analysis by Billant & Chomaz (2000*a*, *b*, *c*) demonstrates a new zigzag instability in strongly stratified fluids, where the dimensional vertical wavelength scales with U/N. The instability appears as a twisting and bending of initially aligned vortex couples and occurred over a narrow band of Froude numbers ($F_{H,dp} = U/NR$, where U and R are the initial convection velocity and radius of the dipole at the onset of instability) between 0.13 and 0.2. For the Lamb–Chaplygin dipole model, analytical vorticity–strain rate relations allowed a matching to be established with the criterion of Miyazaki & Fukumoto (1992) for suppression of the elliptic instability found in homogeneous fluids. In a stratified fluid the resonance between inertio-gravity waves and the imposed strain can occur over a limited band of N, and when N exceeds this value the instability does not grow. Values for an effective maximum critical Froude number, $F_{H,c}$, will vary according to the flow configuration, and the generality of this instability beyond dipoles is currently a matter of conjecture, but the dipole model might be a reasonable generic building block for elements in the late wake. Experimentally, the lower limit for growth of the zigzag instability is a function of the experiment size and limited Reynolds number and is due to viscous dissipation. Numerical experiments (Billant & Chomaz 2000*c*) that avoid this ‘viscous doom’ showed a stabilization of the zigzag mode at a lower value of $F_{H,dp} = 0.05$.

The physical mechanism for the zigzag mode requires only a lateral displacement of a vertically coherent dipole structure. The resulting vertical pressure gradient distorts the isopycnal surfaces, and a vertical velocity field is required to conserve density. The vertical velocity field in turn provides a strain field on the vertical vorticity, stretching it, which then induces secondary horizontal motions to increase the deflection in the direction of the original displacement. In principle, this physical mechanism could operate in the late wake. The range of measurable F_H in figure 15(*e*) from 0.3 to

F	4	16	64
l_o	1.6	1.3	1.0
l_{zz}	1.8	1.5	1.2
l_V	2.1	3.1	2.3
(Nt)	3.5	12	11
F_{loc}	0.8	0.8	0.8

TABLE 2. Vertical scales (in cm) at Nt_c as predicted by Osmidov-type criteria (l_o) and the zigzag criterion (l_{zz}). l_V, the measured layer height is determined at the noted Nt and most likely has uncertainty of ±0.5 cm. F_{loc} is set by l_c and u_c, as discussed in the text.

0.04 matches that of growing zigzag modes quite well, and the small but non-zero w velocity component (figure 12) has already been noted. The prediction is simple: the zigzag wavelength, l_{zz} scales as U/N. A most interesting corollary is that $F_V = O(1)$, and not $\ll 1$.

Last, Majda & Grote (1997) constructed exact, laminar solutions of the Boussinesq equations in the low Froude number limit, where $w = 0$, and showed analytically that given this approximation, then the increasing contribution of the vertical shear towards the kinetic energy dissipation and the increase in the horizontal vorticity component are necessarily coupled. Collapse of vertical columnar vortices into high-aspect-ratio pancake-like structures was demonstrated in the presence of a mean shear, but the dependence of a characteristic vertical scale on the magnitude of this externally imposed linear shear was not clear. Partly due to the absence of such a uniform external shear, and partly due to the fact that $w \neq 0$ when the vertical scales are apparently established in the wake, application of this intriguing analysis must be restricted to the late, Q2D, wake.

Two plausible, contrasting mechanisms are left for vertical scale selection in the sphere wake. One is a constraint on local overturning scales in turbulent flow, while the other is a laminar instability of initially columnar vortices. Power laws for general length, l, and velocity, u, scales can be expressed as a function of x/D:

$$\frac{l}{D} \simeq C_1 \left(\frac{x}{D}\right)^{C_2}, \quad \frac{u}{U} \simeq C_3 \left(\frac{x}{D}\right)^{C_4}.$$

Setting $l = L_V$ and $u = U_0$, the values of the constants C_{1-4} can be taken from the homogeneous wake data in figure 9. At $Nt = (x/D)(2/F) \approx 2$, numerical values can be calculated for these scales at collapse, l_c and u_c. These are then used to calculate l_0 from (1.6) and the zigzag scale from $l_{zz} = u_c/N$. Table 2 shows the predicted and measured vertical length scales at Nt_c.

The earliest measurable values of l_V do not vary appreciably with F, while both l_o and l_{zz} decrease slightly as a consequence of the increasing effective x/D at Nt_c. The predicted l_o and l_{zz} are very close, and it would be difficult, in principle, to distinguish experimentally between them. Both l_o and l_{zz} underpredict the measured l_V, although only marginally beyond experimental uncertainty. It could be argued that, based on the observed non-uniformity of the vertical structure at early times (figure 6), then a local turbulence length scale argument ought to be more applicable. If so, it would prevent the simultaneous appearance of a zigzag mode due to the lack of initial vertical coherence and the weak wavelength selection in the unforced zigzag (Billant & Chomaz 2000*a*). Later on, since $u \sim (Nt)^{-2/3}$, then l_{zz} will also decrease to become small compared with the initially established, and comparatively constant, l_V. Zigzags could still grow within each layer, where the vortex lines might be vertically coherent. Yet, by $Nt \approx 50$, the local Froude number based on horizontal scales, F_H, (figure 15*c*) has dropped to approximately 0.05, when Billant & Chomaz (2000*a*) reported viscous extinction of the instability in laboratory experiments. The zigzag is thus presented with a vanishing window of opportunity, closed on one side by the early generation of preferred scales by turbulent overturning mechanisms, and on the other by the increasingly dominant influence of buoyancy and/or viscosity.

If l_o seems a more likely determinant of the initial and late-wake maximum vertical length scale, the explanation is still not entirely straightforward, because one finds empirically that the best collapse of the individual layer height data has the form

$$\left(\frac{l_V}{D}\right) F^{-1/2} \simeq 0.2 \pm 0.1 (Nt)^{0.1 \pm 0.1}.$$

The exponent of 1/2 is different from the 1/3 value predicted in (5.6), which is measurably worse (in terms of minimizing the standard deviation of the constants in the power-law scaling) in collapsing the data. A correct accounting for the observed length scale selection and its variation with F may require the inclusion of the effect of weak forcing by coherent structures established in the early wake (Chomaz *et al.* 1993*b*; Bonneton *et al.* 1996; Spedding 2001), thereby including a dependence on initial conditions.

It should also be recognized that coupled, coherent fluid motions in the horizontal may modify the vertical length scale arguments, although most of the horizontal, late-wake dynamics have been shown to be F-independent. Obviously the emerging and merging of coherent patches of vertical vorticity can be responsible for significant modification of the vertical structure. Vortex merging that occurs in one layer, and that is unaccompanied by a similar merging of its companions above and below will generate significant shearing motion, or horizontal vorticity, as postulated long ago by Lilly (1983), and confirmed experimentally by Fincham *et al.* (1996). It is not known whether the opposite process is common, i.e. a vertical alignment of vortex patches forced through horizontal vortex–vortex interactions. Vertical alignment of patches of relative or potential vorticity in two-layer, quasi-geostrophic models has been discussed by Polvani, Zabusky & Flierl (1989), Verron, Hopfinger & McWilliams (1990), Polvani (1991) and Corréard & Carton (1999), but show significant sensitivity to initial conditions, making extrapolation to current circumstances non-obvious at the very least, even disregarding the lack of strong background rotation.

5.3. *The scaling of decaying stratified turbulence*

Finally, the numerical values of the local Froude numbers in horizontal and vertical directions shed some light on the appropriate scaling for intermediate (NEQ) and late-time (Q2D) wake evolution, with particular reference back to the scaled equations (1.1)–(1.4) in § 1.2. In table 2, a value is given for a local Froude number, F_{loc}, based on l_c and u_c at $Nt_c \approx 2$. Since the turbulent flow is imagined to be oblivious of the stratification up until this point, $F_{loc} = F_V = F_H$. As originally noted by Riley *et al.* (1981), $F_{loc} \approx 1$ at collapse, close to one buoyancy period, and does not depend on F. The original scaling of the equations by Riley *et al.* was based on $F_V \ll 1$, when the vertical and horizontal motions decouple to leading order. The generality of this result has been questioned in the analysis of Billant & Chomaz (2000*b*), who show that when the vertical scale is controlled by a zigzag mode, then $F_V = O(1)$ and the system cannot in this case be approximated by two-dimensional Euler equations.

The correct scaling depends on the aspect ratio, A, of the vortex structures, which in turn relates F_V and F_H. The measured F_V and F_H (figure 12*b*, *c*) begin (at $Nt \approx 10$ in this experiment) at approximately the same order, depending on F, and their ratio (or A) increases with time because F_H decreases faster. F_H decreases more rapidly because horizontal length scales can continue to increase, while vertical scales cannot. The primary mechanism for increasing horizontal length scales is through pairing of like-signed vortices (SBF96). F_V does not maintain its value of order one in the late wake, because the initial vertical length scale, imposed perhaps by a modified Osmidov-type argument, is larger than that predicted by l_{zz}. On the other hand, the wake-averaged vertical velocities are not an order of magnitude smaller than the fluctuating horizontal velocities until $Nt \approx 100$ (figure 9), and $F_V \ll 1$ is only valid in the late Q2D flow.

The length and velocity scales measured in this experiment suggest the need for fully three-dimensional experiments in the future. Just as setting $w = 0$ in theoretical analysis precludes the full range of potential instabilities in the NEQ regime, the correct velocity field cannot be recovered from sequences of horizontal slices alone. Techniques using interlaced orthogonal planes seem promising and are being investigated.

This paper includes data from much diligent and careful work conducted by graduate students Robert Bell and Jun Chen. Professor F. K. Browand provided his customary thoughtful and constructive comments throughout, and read an earlier version of the manuscript. We are all most grateful to Dr L. P. Purtell for support on ONR Grant# N00014-96-1-1001.

REFERENCES

Beckers, M., Verzicco, R., Clercx, H. J. H. & van Heijst, G. J. F. 2001 The vertical structure of pancake-like vortices in a stratified fluid: experiments, model and numerical simulations. *J. Fluid Mech.* **433**, 1–27.

Bevilaqua, P. M. & Lykoudis, P. S. 1978 Turbulence memory in self-preserving wakes. *J. Fluid Mech.* **89**, 589–606.

Billant, P. & Chomaz, J.-M. 2000*a* Experimental evidence for a new instability of a vertical columnar vortex pair in a strongly stratified fluid. Part 1. *J. Fluid Mech.* **418**, 167–188.

Billant, P. & Chomaz, J.-M. 2000*b* Theoretical analysis of the zigzag instability of a vertical columnar vortex pair in a strongly stratified fluid. *J. Fluid Mech.* **419**, 29–63.

Billant, P. & Chomaz, J.-M. 2000*c* Three-dimensional stability of a vertical columnar vortex pair in a stratified fluid. *J. Fluid Mech.* **419**, 65–91.

Bonneton, P., Chomaz, J.-M. & Hopfinger, E. J. 1993 Internal waves produced by the turbulent wake of a sphere moving horizontally in a stratified fluid. *J. Fluid Mech.* **254**, 23–40.

Bonneton, P., Chomaz, J.-M., Hopfinger, E. J. & Perrier, M. 1996 The structure of the turbulent wake and the random wave field generated by a moving sphere in a stratified fluid. *Dyn. Atmos. Oceans* **23**, 299–308.

Browand, F. K., Guyomar, D. & Yoon, S. C. 1987 The behaviour of a turbulent front in a stratified fluid: experiments with an oscillating grid. *J. Geophys. Res.* **92**, 5329–5341.

Chomaz, J.-M., Bonneton, P., Butet, A. & Hopfinger, E. J. 1993*a* Vertical diffusion in the far wake of a sphere moving in a stratified fluid. *Phys. Fluids* A **5**, 2799–2806.

Chomaz, J.-M., Bonneton, P. & Hopfinger, E. J. 1993*b* The structure of the near wake of a sphere moving horizontally in a stratified fluid. *J. Fluid Mech.* **254**, 1–21.

Corréard, S. M. & Carton, X. J. 1999 Vertical alignment of geostrophic vortices: on the influence of the initial distribution of potential vorticity. In *Simulation and Identification of Organised Structures in Flows: Proc. IUTAM Symp.* (ed. J. N. Sorensen, E. J. Hopfinger & N. Aubry), pp. 191–200. Kluwer.

Dallmann, U. C., Vollmers, H. & Su, W. 1999 Flow topology and tomography for vortex identification in unsteady and three-dimensional flows. In *Simulation and Identification of*

Organized Structures in Flows: Proc. IUTAM Symp. (ed. J. N. Sorensen, E. J. Hopfinger & N. Aubry), pp. 223–233. Kluwer.

Dritschel, D. G. & de la Torre Juárez, M. 1996 The instability and breakdown of tall columnar vortices in a quasi-geostrophic fluid. *J. Fluid Mech.* **328**, 129–160.

Dritschel, D. G., de la Torre Juárez, M. & Ambaum, M. H. P. 1999 The three-dimensional vortical nature of atmospheric and oceanic turbulent flows. *Phys. Fluids* **11**, 1512–1520.

Embid, P. F. & Majda, A. J. 1998 Low froude number limiting dynamics for stably stratified flows with small or finite Rossby numbers. *Geophys. Astrophys. Fluid Dyn.* **87**, 1–50.

Fincham, A. M., Maxworthy, T. & Spedding, G. R. 1996 Energy dissipation and vortex structure in freely-decaying, stratified grid turbulence. *Dyn. Atmos. Oceans* **23**, 155–169.

Fincham, A. M. & Spedding, G. R. 1997 Low-cost, high-resolution DPIV for turbulent flows. *Exps. Fluids* **23**, 449–462.

Gibson, C. H. 1986 Internal waves, fossil turbulence, and composite ocean microstructure spectra. *J. Fluid Mech.* **168**, 89–117.

Gibson, C. H. 1991 Laboratory, numerical, and oceanic fossil turbulence in rotating and stratified flows. *J. Geophys. Res.* **96**, C7, 12549–12566.

Gibson, C. H., Chen, C. C. & Lin, S. C. 1968 Measurements of turbulent velocity and temperature fluctuations in the wake of a sphere. *AIAA J.* **6**, 642–649.

Gilreath, H. E. & Brandt, A. 1985 Experiments on the generation of internal waves in a stratified fluid. *AIAA J.* **23**, 693–700.

Herring, J. R. & Métais, O. 1989 Numerical experiments in forced stably stratified turbulence. *J. Fluid Mech.* **202**, 97–115.

Hopfinger, E. J. 1987 Turbulence in stratified fluids: a review. *J. Geophys. Res.* **92**, 5287–5303.

Hopfinger, E. J., Flór, J. B., Chomaz, J.-M. & Bonneton, P. 1991 Internal waves generated by a moving sphere and its wake in a stratified fluid. *Exps. Fluids* **11**, 255–261.

Jacobitz, F. G., Sarkar, S. & Van Atta, C. W. 1997 Direct numerical simulations of the turbulence evolution in a uniformly sheared and stably stratified flow. *J. Fluid Mech.* **342**, 231–261.

Kimura, Y. & Herring, J. R. 1996 Diffusion in stably stratified turbulence. *J. Fluid Mech.* **328**, 253–269.

Lelong, M.-P. & Riley, J. J. 1991 Internal wave–vortical mode interactions in strongly stratified flows. *J. Fluid Mech.* **232**, 1–19.

Lilly, D. K. 1983 Stratified turbulence and the mesoscale variability of the atmosphere. *J. Atmos. Sci.* **40**, 749–761.

Lin, J. T. & Pao, Y. H. 1979 Wakes in stratified fluids: a review. *Annu. Rev. Fluid Mech.* **11**, 317–338.

Lin, Q., Lindberg, W. R., Boyer, D. L. & Fernando, H. J. S. 1992 Stratified flow past a sphere. *J. Fluid Mech.* **240**, 315–354.

Liu, Y. N., Maxworthy, T. & Spedding, G. R. 1987 Collapse of a turbulent front in stratified fluid 1. Nominally two-dimensional evolution in a narrow tank. *J. Geophys. Res.* **92**, 5427–5433.

Majda, A. J. & Grote, M. J. 1997 Model dynamics and vertical collapse in decaying strongly stratified flows. *Phys. Fluids* **9**, 2932–2940.

McWilliams, J. C. 1984 The emergence of isolated coherent vortices in turbulent flow. *J. Fluid Mech.* **146**, 21–43.

McWilliams, J. C., Weiss, J. B. & Yavneh, I. 1994 Anisotropy and coherent vortex structures in planetary turbulence. *Science* **264**, 410–999.

Métais, O. & Herring, J. R. 1989 Numerical simulations of freely evolving turbulence in stably stratified fluids. *J. Fluid Mech.* **202**, 117–148.

Miyazaki, T. & Fukumoto, Y. 1992 Three-dimensional instability of strained vortices in a stably stratified fluid. *Phys. Fluids* A **4**, 2515–2522.

Park, Y. G., Whitehead, J. A. & Gnadadeskian, A. 1994 Turbulent mixing in stratified fluids: layer formation and energetics. *J. Fluid Mech.* **279**, 279–311.

Polvani, L. M. 1991 Two-layer geostrophic vortex dynamics. Part 2. Alignment and two-layer V-states. *J. Fluid Mech.* **225**, 241–270.

Polvani, L. M., Zabusky, N. J. & Flierl, G. R. 1989 Two-layer geostrophic vortex dynamics. Part 1. Upper-layer V-states and merger. *J. Fluid Mech.* **205**, 215–242.

Riley, J. J. & Lelong, M.-P. 2000 Fluid motions in the presence of strong stable stratification. *Annu. Rev. Fluid Mech.* **32**, 613–657.

Riley, J. J., Metcalfe, R. W. & Weissman, M. A. 1981 Direct numerical simulations of homogeneous turbulence in density stratified fluids. In *Nonlinear Properties of Internal Waves* (ed. B. J. West), pp. 79–112. New York: AIP.

Spedding, G. R. 1997 The evolution of initially-turbulent bluff-body wakes at high internal Froude number. *J. Fluid Mech.* **337**, 283–301 (referred to herein as Sp97).

Spedding, G. R. 1999 Vortex wakes in stably-stratified fluids. In *Simulation and Identification of Organised Structures in Flows: Proc. IUTAM Symp.* (ed. J. N. Sorensen, E. J. Hopfinger & N. Aubry), pp. 163–179. Kluwer.

Spedding, G. R. 2001 Anisotropy in turbulence profiles of stratified wakes. *Phys. Fluids* **13**, 2361–2372.

Spedding, G. R., Browand, F. K., Bell, R. & Chen, J. 2000 Internal waves from intermediate, or late-wake vortices. In *Stratified Flows I: Proc. 5th Intl Symp. on Stratified Flows, Vancouver, Canada:* (ed. G. A. Lawrence, R. Pieters & N. Yonemitsu), pp. 113–118. UBC.

Spedding, G. R., Browand, F. K. & Fincham, A. M. 1996*a* The long-time evolution of the initially-turbulent wake of a sphere in a stable stratification. *Dyn. Atmos. Oceans* **23**, 171–182.

Spedding, G. R., Browand, F. K. & Fincham, A. M. 1996*b* Turbulence, similarity scaling and vortex geometry in the wake of a sphere in a stably-stratified fluid. *J. Fluid Mech.* **314**, 53–103 (referred to herein as SBF96).

Staquet, C. & Riley, J. J. 1989 On the velocity field associated with potential vorticity. *Dyn. Atmos. Oceans* **14**, 93–99.

Sysoeva, E. Y. & Chashechkin, Y. D. 1991 Vortex systems in the stratified wake of a sphere. *Izv. Akad. Nauk SSSR, Mekh. Zhidk. Gaza* **4**, 82–90.

Thoroddsen, S. T. & Van Atta, C. W. 1993 Experimental study of the effects of grid configuration on the dynamical evolution of decaying turbulence in a stably stratified fluid. *Dyn. Atmos. Oceans* **19**, 259–288.

Uberoi, M. S. & Freymuth, P. 1970 Turbulent energy balance and spectra of the axisymmetric wake. *Phys. Fluids* **13**, 2205–2210.

Verron, J., Hopfinger, E. J. & McWilliams, J. C. 1990 Sensitivity to initial conditions in the merging of two-layer baroclinic vortices. *Phys. Fluids* **2**, 886–889.

Voropayev, S. I. & Afanasyev, Y. D. 1994 *Vortex Structures in a Stratified Fluid*. Chapman & Hall.

Voropayev, S. I., Afanasyev, Y. D. & Filippov, I. A. 1991 Horizontal jets and vortex dipoles in a stratified fluid. *J. Fluid Mech.* **227**, 543–566.